The Astrophysical Journal Letters, 988:L13 (19pp), 2025 July 20 https://doi.org/10.3847/2041-8213/ade7f9

EP 250108a/SN 2025kg: Observations of the Most Nearby Broad-line Type Ic Supernova Following an Einstein Probe Fast X-Ray Transient

Jillian C. Rastinejad[1], Andrew J. Levan[2,3], Peter G. Jonker[2], Charles D. Kilpatrick[1], Christopher L. Fryer[4], Nikhil Sarin[5,6], Benjamin P. Gompertz[7,8], Chang Liu[1], Rob A. J. Eyles-Ferris[9], Wen-fai Fong[1], Eric Burns[10], James H. Gillanders[11], Ilya Mandel[12,13], Daniele Bjørn Malesani[14,15], Paul T. O'Brien[9], Nial R. Tanvir[9], Kendall Ackley[3], Amar Aryan[16], Franz E. Bauer[17], Steven Bloemen[2], Thomas de Boer[18], Clécio R. Bom[19], Jennifer A. Chacón[20,21], Ken Chambers[18], Ting-Wan Chen[16], Ashley A. Chrimes[2,22], Joyce N. D. van Dalen[2], Valerio D'Elia[23], Massimiliano De Pasquale[24], Michael D. Fulton[25], Paul J. Groot[2,26,27], Rahul Gupta[28,53], Dieter H. Hartmann[29], Agnes P. C. van Hoof[2], Mark E. Huber[18], Luca Izzo[30,31], Wynn Jacobson-Galan[32,54], Páll Jakobsson[33], Albert Kong[34], Tanmoy Laskar[2,35], Thomas B. Lowe[36], Eugene A. Magnier[37], Elisabetta Maiorano[38], Antonio Martin-Carrillo[39], Lluis Mas-Ribas[40,41], Daniel Mata Sánchez[42,43], Matt Nicholl[25], Christopher J. Nixon[44], Samantha R. Oates[45], Gregory Paek[18], Jesse Palmerio[46], Diego Paris[47], Daniëlle L. A. Pieterse[2], Giovanna Pugliese[48], Jonathan A. Quirola Vasquez[2], Jan van Roestel[49], Andrea Rossi[38], Alicia Rouco Escorial[22], Ruben Salvaterra[50], Benjamin Schneider[51], Stephen J. Smartt[11,25], Ken Smith[11,25], Ian A. Smith[18], Shubham Srivastav[11], Manuel A. P. Torres[42,43], Chiara Ventura[47], Paul Vreeswijk[2], Richard Wainscoat[18], Yi-Jung Yang[16], and Sheng Yang[52]

[1] Center for Interdisciplinary Exploration and Research in Astrophysics (CIERA) and Department of Physics and Astronomy, Northwestern University, Evanston, IL 60208, USA; jillianrastinejad2024@u.northwestern.edu
[2] Department of Astrophysics/IMAPP, Radboud University, 6525 AJ Nijmegen, The Netherlands
[3] Department of Physics, University of Warwick, Coventry CV4 7AL, UK
[4] Center for Nonlinear Studies, Los Alamos National Laboratory, Los Alamos, NM 87545, USA
[5] The Oskar Klein Centre, Department of Physics, Stockholm University, AlbaNova, SE-106 91 Stockholm, Sweden
[6] Nordita, Stockholm University and KTH Royal Institute of Technology, Hannes Alfvéns väg 12, SE-106 91 Stockholm, Sweden
[7] School of Physics and Astronomy, University of Birmingham, Birmingham B15 2TT, UK
[8] Institute for Gravitational Wave Astronomy, University of Birmingham, Birmingham B15 2TT, UK
[9] School of Physics and Astronomy, University of Leicester, University Road, Leicester LE1 7RH, UK
[10] Department of Physics and Astronomy, Louisiana State University, Baton Rouge, LA 70803, USA
[11] Astrophysics sub-Department, Department of Physics, University of Oxford, Keble Road, Oxford OX1 3RH, UK
[12] School of Physics and Astronomy, Monash University, Clayton, VIC 3800, Australia
[13] ARC Centre of Excellence for Gravitational-wave Discovery (OzGrav), Melbourne, Australia
[14] Cosmic Dawn Center (DAWN), Denmark
[15] Niels Bohr Institute, University of Copenhagen, Jagtvej 128, Copenhagen 2200, Denmark
[16] Graduate Institute of Astronomy, National Central University, 300 Jhongda Road, 32001 Jhongli, Taiwan
[17] Instituto de Alta Investigación, Universidad de Tarapacá, Casilla 7D, Arica, Chile
[18] Institute for Astronomy, University of Hawaii, 2680 Woodlawn Drive, Honolulu, HI 96822, USA
[19] Centro Brasileiro de Pesquisas Físicas, Rua Dr. Xavier Sigaud 150, 22290-180 Rio de Janeiro, RJ, Brazil
[20] Instituto de Astrofísica, Facultad de Física, Pontificia Universidad Católica de Chile, Campus San Joaquín, Av. Vicuña Mackenna 4860, Macul Santiago,7820436, Chile
[21] Millennium Institute of Astrophysics, Nuncio Monseñor Sótero Sanz 100, Of 104, Providencia, Santiago, Chile
[22] European Space Agency (ESA), European Space Astronomy Centre (ESAC), Camino Bajo del Castillo s/n, 28692 Villanueva de la Cañada, Madrid, Spain
[23] Space Science Data Center (SSDC)—Agenzia Spaziale Italiana (ASI), I-00133 Roma, Italy
[24] Department of Mathematics and Computer Sciences, Physical Sciences and Earth Sciences, University of Messina, Via F. S. D'Alcontres 31, 98166 Messina, Italy
[25] Astrophysics Research Centre, School of Mathematics and Physics, Queen's University Belfast, Belfast BT7 1NN, UK
[26] Department of Astronomy, University of Cape Town, Private Bag X3, Rondebosch 7701, South Africa
[27] South African Astronomical Observatory, P.O. Box 9, Observatory 7935, South Africa
[28] Astrophysics Science Division, NASA Goddard Space Flight Center, Mail Code 661, Greenbelt, MD 20771, USA
[29] Clemson University, Department of Physics & Astronomy, Clemson, SC 29631, USA
[30] INAF—Osservatorio Astronomico di Capodimonte, Salita Moiariello 16, I-80131 Napoli, Italy
[31] DARK, Niels Bohr Institute, University of Copenhagen, Jagtvej 155, 2200 Copenhagen N, Denmark
[32] Department of Astronomy and Astrophysics, California Institute of Technology, Pasadena, CA 91125, USA
[33] Center for Astrophysics and Cosmology, Science Institute, University of Iceland, Dunhagi 5, 107 Reykjavik, Iceland
[34] Institute of Astronomy, National Tsing Hua University, Hsinchu 30013, Taiwan
[35] Department of Physics & Astronomy, University of Utah, Salt Lake City, UT 84112, USA
[36] University of Hawaii, Institute for Astronomy, 34 Ohia Ku Street, Makawao, HI 96768, USA
[37] Institute for Astronomy, University of Hawai'i at Manoa, 2680 Woodlawn Drive, Honolulu, HI 96822, USA
[38] INAF—Osservatorio di Astrofisica e Scienza dello Spazio, Via Piero Gobetti 93/3, I-40129 Bologna, Italy
[39] School of Physics and Centre for Space Research, University College Dublin, Belfield, Dublin 4, Ireland
[40] Department of Astronomy and Astrophysics, University of California, 1156 High Street, Santa Cruz, CA 95064, USA
[41] University of California Observatories, 1156 High Street, Santa Cruz, CA 95064, USA
[42] Instituto de Astrofísica de Canarias, E-38205 La Laguna, Tenerife, Spain
[43] Departamento de Astrofísica, University de La Laguna, E-38206 La Laguna, Tenerife, Spain
[44] School of Physics and Astronomy, Sir William Henry Bragg Building, Woodhouse Ln., University of Leeds, Leeds LS2 9JT, UK
[45] Department of Physics, Lancaster University, Lancaster LA1 4YB, UK
[46] Université Paris-Saclay, Université Paris Cité, CEA, CNRS, AIM, 91191 Gif-sur-Yvette, France
[47] INAF—Osservatorio Astronomico di Roma, Via Frascati 33, I-00040 Monte Porzio Catone, Italy
[48] Astronomical Institute Anton Pannekoek, University of Amsterdam, 1090 GE Amsterdam, The Netherlands
[49] Anton Pannekoek Institute for Astronomy, University of Amsterdam, 1090 GE Amsterdam, The Netherlands

[50] INAF—Istituto di Astrofisica Spaziale e Fisica Cosmica di Milano, Via A. Corti 12, 20133 Milano, Italy
[51] Aix Marseille University, CNRS, CNES, LAM, Marseille, France
[52] Institute for Gravitational Wave Astronomy, Henan Academy of Sciences, Zhengzhou 450046, Henan, People's Republic of China
Received 2025 April 11; revised 2025 June 17; accepted 2025 June 17; published 2025 July 16

Abstract

With a small sample of fast X-ray transients (FXTs) with multiwavelength counterparts discovered to date, their progenitors and connections to γ-ray bursts (GRBs) and supernovae (SNe) remain ambiguous. Here, we present photometric and spectroscopic observations of SN 2025kg, the SN counterpart to the FXT EP 250108a. At $z = 0.17641$, this is the closest known SN discovered following an Einstein Probe (EP) FXT. We show that SN 2025kg's optical spectra reveal the hallmark features of a broad-lined Type Ic SN. Its light-curve evolution and expansion velocities are comparable to those of GRB-SNe, including SN 1998bw, and two past FXT-SNe. We present JWST/NIRSpec spectroscopy taken around SN 2025kg's maximum light, and find weak absorption due to He I 1.0830 μm and 2.0581 μm and a broad, unidentified emission feature at $\sim$4–4.5 μm. Further, we observe broadened Hα in optical data at 42.5 days that is not detected at other epochs, indicating interaction with H-rich material. From its light curve, we derive a ^{56}Ni mass of 0.2–0.6 $M_\odot$. Together with our companion Letter, our broadband data are consistent with a trapped or low-energy ($\lesssim 10^{51}$ erg) jet-driven explosion from a collapsar with a zero-age main-sequence mass of 15–30 $M_\odot$. Finally, we show that the sample of EP FXT-SNe supports past estimates that low-luminosity jets seen through FXTs are more common than successful (GRB) jets, and that similar FXT-like signatures are likely present in at least a few percent of the brightest Type Ic-BL SNe.

Unified Astronomy Thesaurus concepts: Core-collapse supernovae (304); Gamma-ray bursts (629); X-ray transient sources (1852)

Materials only available in the online version of record: machine-readable table

1. Introduction

Though first discovered in the era of sounding rockets (e.g., B. A. Cooke 1976), and highlighted by discoveries with Chandra and XMM-Newton (P. G. Jonker et al. 2013; D. Alp & J. Larsson 2020; J. Quirola-Vásquez et al. 2023), the nature of fast X-ray transients (FXTs; nonrepeating transients detected in the X-ray) and their connection to the deaths of massive stars and luminous, jetted γ-ray bursts (GRBs) remains uncertain. By definition, FXTs represent a broad category of transients. In some cases, FXTs could represent the tail of the emission from classical GRBs whose spectra peak at tens to hundreds of kiloelectronvolts. FXTs also encompass the population of so-called X-ray flashes (XRFs; J. Heise et al. 2001; T. Sakamoto et al. 2005), a historical subtype of GRBs defined by a greater ratio of fluence in the X-ray compared to the γ-ray bands. Most notably, this XRF/FXT group includes the nearby, serendipitous discoveries of Type Ib/c supernovae (SNe), SN 2006aj (S. Campana et al. 2006; E. Pian et al. 2006; A. M. Soderberg et al. 2006) identified in the long GRB/XRF 060218 and the X-ray-only discovery of the much less luminous SN 2008D (A. M. Soderberg et al. 2008). These discoveries showed that at least some FXTs are produced by the core collapse of massive, stripped-envelope stars. Though sharing similarities with the broad-line Type Ic (Ic-BL) SNe accompanying GRBs (GRB-SNe), the SNe associated with XRFs demonstrate considerable diversity compared to GRB-SNe. For example, two SNe (SN 2008D and SN 2010bh; A. M. Soderberg et al. 2008) following these XRFs were $\approx$5–100 times less luminous compared to the prototypical GRB-SN, GRB 980425/SN 1998bw. Further, one (SN 2008D) showed absorption due to He (A. M. Soderberg et al. 2006; M. Modjaz et al. 2009), potentially representing a stage in the continuum of massive star explosions (e.g., T. J. Galama et al. 1998; A. M. Soderberg et al. 2008; A. Clocchiatti et al. 2011; D. Alp & J. Larsson 2020). However, with a limited sample of such events to date, the mapping of GRBs to FXTs, XRFs, or core-collapse SNe without high-energy emission continues to be an open question.

Previously, the lack of a dedicated discovery mission meant that the FXT sample was limited to rare, serendipitous detections (e.g., A. M. Soderberg et al. 2006, 2008) or archival searches in narrow-field instruments such as Chandra or XMM-Newton (P. G. Jonker et al. 2013; A. Glennie et al. 2015; F. E. Bauer et al. 2017; D. Alp & J. Larsson 2020; G. Novara et al. 2020; D. Lin et al. 2022; J. Quirola-Vásquez et al. 2022, 2023). The small ($\lesssim$40) population size of FXTs and paucity of multiwavelength counterparts resulted in large uncertainties on their rates, local environments, and counterpart properties. Uncertainties on these properties inhibit a full understanding of how FXTs fit within the landscape of transients. In particular, many events discovered in the narrow-field searches were of long duration (hundreds to thousands of seconds) compared to GRBs. At present, it is unclear if these long durations represent a selection effect or fundamentally different physical processes (e.g., A. J. Levan et al. 2024b). At the same time, the realization of substantial diversity in the progenitors of long GRBs, including events likely produced by compact object mergers (e.g., J. C. Rastinejad et al. 2022; E. Troja et al. 2022; J. Yang et al. 2022; A. J. Levan et al. 2024a), erases the assumption that FXTs arise exclusively via core collapse.

The 2024 launch of a wide-field soft X-ray monitor on board the Einstein Probe (EP), opened a new route to discover FXTs and characterize their multiwavelength counterparts (W. Yuan et al. 2015, 2022). Critically, EP is able to detect FXTs with its Wide Field X-ray Telescope (WXT; 3600 deg^2 field of view),

[53] NASA Postdoctoral Program Fellow.
[54] NASA Hubble Fellow.

localize them via WXT to $\sim 3'$ precision, and subsequently repoint a narrow-field follow-up telescope to obtain $\sim 10''$ position. As such, the latency of FXT announcements has reduced from days (and, often, year timescales) to minutes (e.g., W. J. Zhang et al. 2024; R. Z. Li et al. 2025a). This speed increase offers the unprecedented ability to locate multi-wavelength counterparts and unveil their origins.

In its first year alone, EP discovered dozens of extragalactic FXTs, revealing a diversity of counterparts and environments. While several FXTs have been associated with GRBs (e.g., D. Frederiks et al. 2024; Y.-H. I. Yin et al. 2024; Y. Liu et al. 2025), others have no observed prompt GRB counterpart despite constraints from γ-ray facilities, prompting speculation that their progenitors are distinct from GRBs produced following core collapse (e.g., J. S. Bright et al. 2025; H. Sun et al. 2024; M. Busmann et al. 2025; B. O'Connor et al. 2025; J. N. D. van Dalen et al. 2025). At least four EP events are known to originate at redshifts $z > 3.5$ (A. Bochenek et al. 2024; A. J. Levan et al. 2024b, 2024c; Y. Liu et al. 2025), representing an exciting new path to exploring the distant Universe but limiting detailed studies of multiwavelength counterparts. Notably, the counterpart of EP 240414a was localized to a galaxy at $z = 0.401$ and revealed the spectroscopic signatures of a Type Ic-BL SN. Critically, this event established that at least some EP FXTs originate from the explosions of massive stars (H. Sun et al. 2024; J. N. D. van Dalen et al. 2025). However, at this redshift, late-time spectroscopic and photometric follow-up of the SN was limited (H. Sun et al. 2024; S. Srivastav et al. 2025; J. N. D. van Dalen et al. 2025). More recently, the event EP 250207b was potentially associated with a galaxy at $z = 0.082$ (A. J. Levan et al. 2025a). However, at present, no evidence of an SN counterpart has been announced and published observational limits appear to rule out an SN (Y.-H. Yang et al. 2025).

On 2025 January 8 at 12:30:28.34 UT, EP discovered a new FXT, EP 250108a, with a duration of $\sim 960^{+3092}_{-208}$ s (R. Z. Li et al. 2025a; W. X. Li et al. 2025b). Later analysis of Fermi-GBM observations place a conservative, sky-averaged upper limit on associated emission in the 10–1000 keV band of $f_\gamma < 2.6 \times 10^{-8}$ erg cm^{-2} s^{-1} at 415 s following the initial trigger (Fermi's view of the localization was occulted by Earth prior to this time; M. E. Ravasio et al. 2025). Prompt follow-up observations were not taken, but imaging obtained ~ 1.5 days after the outburst revealed a blue and rapidly fading counterpart with a redshift of $z = 0.17641$ (R. A. J. Eyles-Ferris et al. 2025). Beginning at ≈ 6 days following the initial trigger, the cooling, optical counterpart began to rise in brightness. Spectra taken by the Nordic Optical Telescope (NOT) and Gemini-North at $\delta t \sim 10$ days (where δt refers to the observer-frame time since the EP trigger) showed the signatures of a Type Ic-BL SN, dubbed SN 2025kg (see Section 2.2 for further analysis; A. J. Levan et al. 2025b; G. P. Srinivasaragavan et al. 2025; D. Xu et al. 2025). SN 2025kg offers a unique first opportunity for a detailed comparison between the multiband light curves and spectroscopic properties of FXT-SNe, GRB-SNe, and stripped-envelope SNe observed without high-energy counterparts, shedding light on FXT progenitors.

Here, we present optical and infrared observations and analysis of SN 2025kg, including James Webb Space Telescope (JWST) spectroscopy. This work represents a companion Letter to R. A. J. Eyles-Ferris et al. (2025), which contains an in-depth analysis of the early ($\lesssim 6$ days posttrigger) observations as well as analysis of the radio and high-energy data. In Section 2 we detail our extensive photometric and spectroscopic campaign to characterize SN 2025kg. In Section 3 we analyze our observations, highlight key features in the JWST spectrum, and compare the properties of SN 2025kg to those of past stripped-envelope SNe associated with FXTs, GRBs, and discovered without high-energy triggers. In Section 4 we describe our photometric modeling of SN 2025kg. In Section 5, we infer properties of the progenitor from our observations, including its zero-age main-sequence (ZAMS) mass, constraints on an He shell due to common envelope mass ejection, and contextualize FXT-SNe in the wider population of Type Ic-BL SNe. Throughout this work, we assume a Planck cosmology, (Planck Collaboration et al. 2020) report all magnitudes in the AB system, and assume an event redshift of $z = 0.17641 \pm 0.0003$ (R. A. J. Eyles-Ferris et al. 2025).

2. Observations

2.1. Photometry

Here, we present optical and near-infrared (near-IR) photometry of SN 2025kg covering $6 < \delta t < 66.5$ days (observed frame; observations at $\delta t \lesssim 6$ days are presented in R. A. J. Eyles-Ferris et al. 2025). We obtained optical observations with the Alhambra Faint Object Spectrograph and Camera (ALFOSC) on the NOT, the IO:O on the Liverpool Telescope (LT), the Gemini Multi-Object Spectrographs (GMOS) on the Gemini-North and -South Telescopes, Pan-STARRS, BlackGEM (for q-band description see P. J. Groot et al. 2024), the Multi-Object Double-beam Spectrograph (MODS) on the Large Binocular Telescope (LBT), the Goodman spectrograph on the Southern Astrophysical Research (SOAR) Telescope, the Lulin Observatory, MegaCam on the Canada–France–Hawaii Telescope (CFHT), and T80S-Cam on T80S. All optical images were processed using standard techniques, including Gemini DRAGONS (K. Labrie et al. 2019), a custom Python pipeline, POTPyRI,[55] `photpipe` (see A. Rest et al. 2005; A. Santos et al. 2024, for details), a dedicated LBT data reduction pipeline (A. Fontana et al. 2014), a modified version of the `photometry-sans-frustration` package `psf` (M. Nicholl et al. 2023), the `Elixir` pipeline (E. A. Magnier & J. C. Cuillandre 2004), a custom built pipeline,[56] as well as a combination of standard `PyRAF` tasks (Science Software Branch at STScI 2012) and the `LACosmic` task (P. G. van Dokkum 2001).

We obtain photometry directly on each image using a common set of standard stars drawn from Pan-STARRS (H. A. Flewelling et al. 2020). We do not anticipate significant ($\gtrsim 0.6$ mag) contamination from the underlying host galaxy given its faintness relative to the transient as measured in archival Legacy Survey imaging ($g = 23.40 \pm 0.04$ mag, $r = 23.13 \pm 0.02$ mag, $i = 22.99 \pm 0.06$ mag, and $z = 22.89 \pm 0.08$ mag; A. Dey et al. 2019). In addition, we obtained near-IR imaging with FLAMINGOS2 on Gemini-South and the MMT and Magellan Infrared Spectrograph (MMIRS) on the MMT. We process all near-IR images using DRAGONS and POTPyRI and

[55] https://github.com/CIERA-Transients/POTPyRI
[56] https://hdl.handle.net/11296/98q6x4

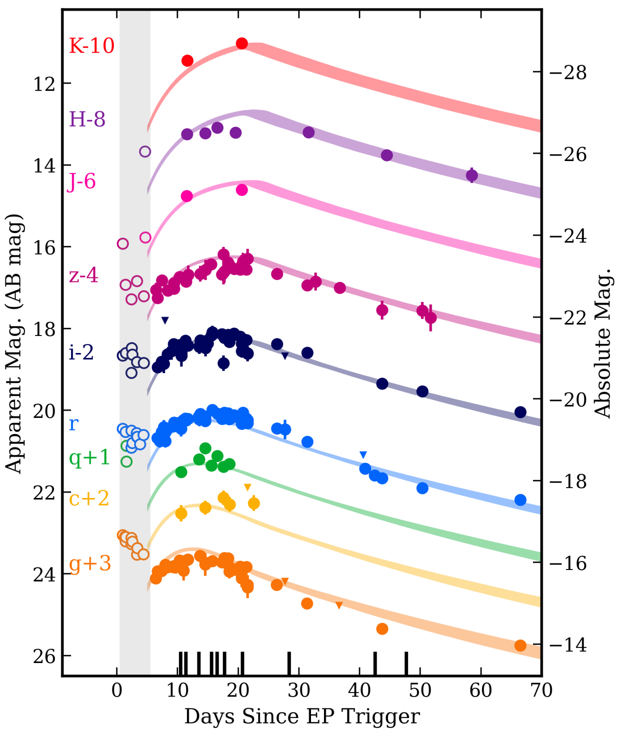

Figure 1. Optical–near-IR detections (circles) and upper limits (triangles) of the counterpart to EP 250108a. The data at $\delta t > 6$ days are well described by a one-zone radioactive decay model (lines; W. D. Arnett 1982; N. Sarin et al. 2024) with a ^{56}Ni mass of $0.6 \pm 0.1\ M_{\odot}$ (Section 4). Observations during the fast-cooling phase prior to the emergence of SN 2025kg ($\delta t < 6$ days; open symbols and gray vertical band) are discussed in detail in R. A. J. Eyles-Ferris et al. (2025). We also show the times of the spectroscopic observations with black vertical lines at the bottom of the figure.

obtain photometry using a common set of standard stars from the Two Micron All Sky Survey (M. F. Skrutskie et al. 2006).

We provide details for all photometric programs in Appendix Table A2. We further incorporate detections from the General Coordinates Network (GCN; A. K. Ror et al. 2025; F. F. Song et al. 2025; X. Zou et al. 2025) and ATLAS forced photometry (*co* bands; J. L. Tonry et al. 2018). We present all photometry in AB magnitudes in Appendix Table A3 and show our observations in Figure 1.

2.2. Spectroscopy

We present 13 optical spectra of SN 2025kg taken over $\delta t = 10.5$–47.7 days. Spectroscopy prior to the emergence of SN features ($2.6 < \delta t < 4.6$ days) is presented and analyzed in our companion Letter (R. A. J. Eyles-Ferris et al. 2025). Our optical spectroscopy was obtained with GMOS on the Gemini-North and -South Telescopes (Program IDs GN-2024B-Q-107, GN-2024B-Q-131, GS-2024B-Q-105, and GS-2025A-Q-107; PIs: Rastinejad and Huber), OSIRIS+ on the Gran Telescopio Canarias (GTC; Program ID GTC1-24ITP; PI: Jonker), the Multi Unit Spectroscopic Explorer (MUSE) on the Very Large Telescope (VLT; Program ID 111.259Q.001; PI: Jonker), and the Low Resolution Imaging Spectrometer (LRIS) on Keck Observatory (PIs: Harrison and Prochaska). Details of each spectroscopic set up are logged in Appendix Table A4.

We reduce Keck and Gemini spectroscopy using `PypeIt` (J. Prochaska et al. 2020). To account for instrumental flexure, subpixel shifts in the position of the [O I] 6300 Å sky emission line were measured and applied as corrections. We reduce the GTC spectra using `Molly` to correct for the Earth's motion relative to the target and observations of spectrophotometric standard stars taken the same night for flux calibration. We reduce the VLT spectrum using ESO-reflex (W. Freudling et al. 2013). We process the LBT spectrum using the Spectroscopic Interactive Pipeline and Graphical Interface tool (A. Gargiulo et al. 2022) and perform wavelength calibration using arc lamp frames. To obtain flux-calibrated LBT spectra, we applied the sensitivity function derived from the spectrophotometric standard star Feige 34. We correct all spectra for Galactic extinction in the direction of the burst ($A_V = 0.049$ mag; E. F. Schlafly & D. P. Finkbeiner 2011) and show the optical spectroscopic series in Figure 2.

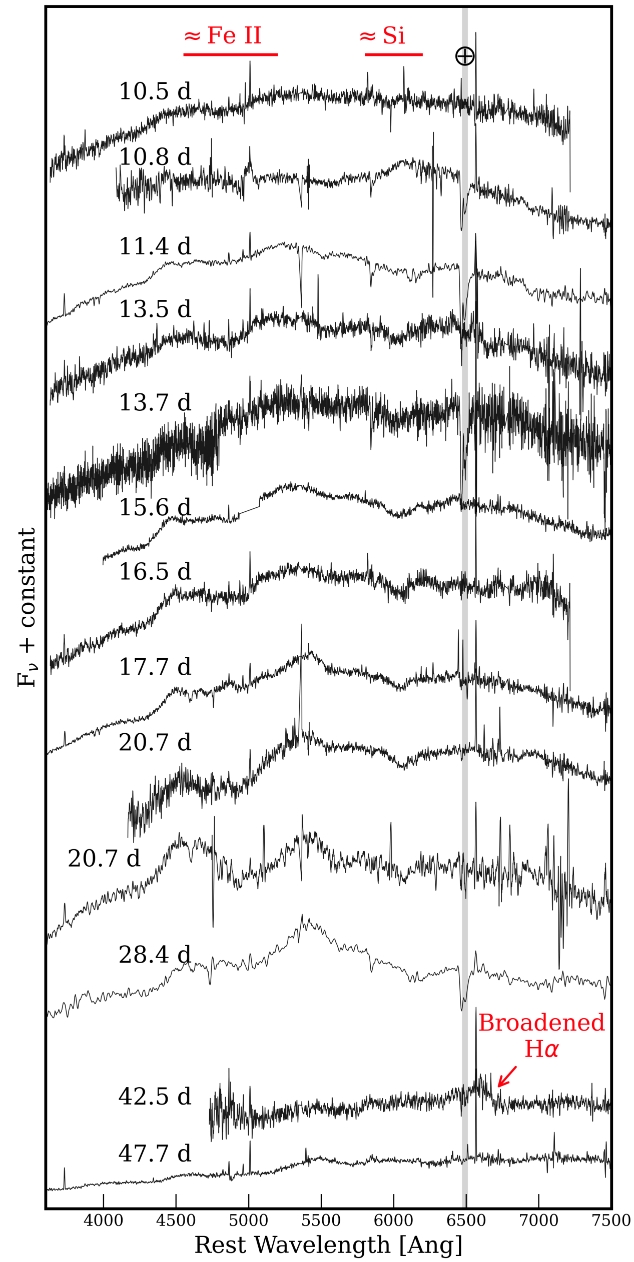

Figure 2. Our spectroscopic sequence of SN 2025kg. We observe broad absorption features around ∼5000 Å and ∼6100 Å that we ascribe to Fe II λ5169 and Si λ6355. In the spectrum at $\delta t = 42.5$ days we observe broadened Hα emission. We mark the location of a telluric feature with a ⊕.

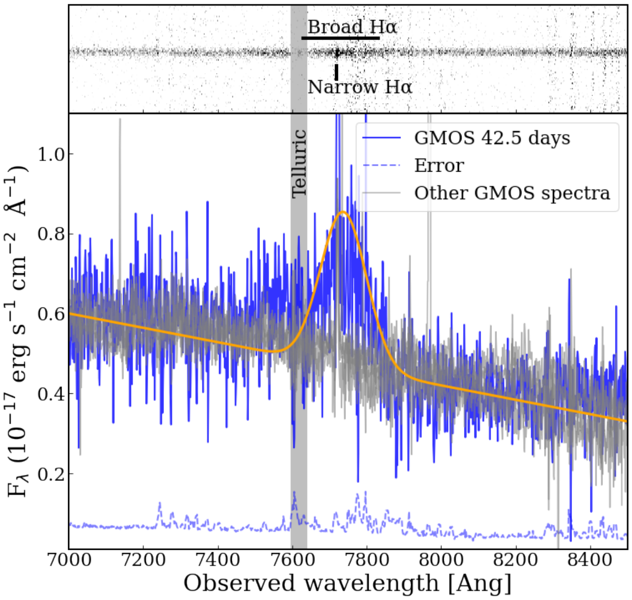

Figure 3. Images of the 2D (top) and 1D (bottom) GMOS spectrum of SN 2025kg taken at δt = 42.5 days, centered around Hα λ6562.8. For comparison, we show our other GMOS spectra in gray, which show only the narrow Hα component. In addition to the narrow component, which is present in other epochs (Figure 2) and likely due to the underlying host galaxy, we observe broad, underlying emission, indicating an H-rich source is interacting with SN 2025kg at this epoch. We show an orange Gaussian superimposed on the continuum for visual purposes.

In each spectrum, we identify the distinct signatures of Type Ic-BL SNe. For instance, we observe at least two broad absorption features around the expected locations of Fe II λ5169 (or a blend of the Fe triplet) and Si λ6355 (Figure 2) and no prominent absorption around the optical features of H or He. In several of the spectra we observe narrow emission lines, including those at the rest-frame locations of Hα, Hβ, and [O III] $\lambda\lambda$4958, 5007, which we attribute to the underlying host galaxy. To compare SN 2025kg to other SNe, we utilize the spectral template matching tool `gelato` (A. H. Harutyunyan et al. 2008), which matches an input spectrum to a large bank of observed SN spectra at a range of phases. For the SN 2025kg spectrum observed at δt = 17.7 days `gelato` finds the Type Ic-BL SN 2006aj (associated with GRB/XRF 060218) at 0.8 days past peak provides the strongest fit. For the SN 2025kg spectrum observed at δt = 28.4 days, `gelato` finds strong matches to several Type Ic-BL SNe, including SNe 1997ef, 1998bw, 2002ap, and 2006aj. This analysis definitively confirms our classification of SN 2025kg as a Type Ic-BL SN.

In the GMOS spectrum at δt = 42.5 days (Figure 3) we observe a broadened Hα emission feature, distinct from the narrow Hα emission observed in previous epochs (Figure 2). We inspected the individual four 2D spectral frames of the δt = 42.5 day spectrum and observe evidence for excess emission associated with this broadened feature in each. We do not see significant broadened Hα emission in the previous (δt = 28.4 days) or subsequent (δt = 47.7 days) spectra. We discuss this feature in greater detail in Section 3.2.

In addition, we obtained two near-IR spectra of SN 2025kg. At δt = 12.7 days postburst we obtained a cross-dispersed spectrum covering 0.82–2.5 μm with the Gemini Near-Infrared Spectrograph (GNIRS) on Gemini-North (Program ID GN-2024B-Q-107; PI: Rastinejad). These data were processed in `Pypeit` with additional postprocessing performed following methods described in S. Tinyanont et al. (2024). Due to a low signal-to-noise ratio (S/N) over the majority of the bandpass, we consider only the portion $\lesssim$1.25 μm usable. Further, at δt = 17.2 days, we obtained fixed slit spectroscopy with NIRSpec on JWST (Program 6133; PI: Gompertz) using the prism (covering 0.5–5 μm) at low resolution, and with an exposure time of 6302 s. At the time of the JWST spectroscopy the source is point-like and several magnitudes brighter than the anticipated magnitude of its compact underlying host galaxy. Therefore, we utilize the default pipeline reduction and 1D extraction of the NIRSpec observations.

3. Analysis and Comparison to Past Events

3.1. Supernova Light Curves

To place SN 2025kg in context of past GRB-SNe, FXT-SNe, and other stripped-envelope SNe, we compare its light curve to those of relevant past events. We include 11 events with X-ray or GRB counterparts: SN 1998bw (GRB 980425; A. Clocchiatti et al. 2011), SN 2003dh (GRB 030329; T. Matheson et al. 2003), SN 2006aj (GRB/XRF 060218; N. Mirabal et al. 2006; A. M. Soderberg et al. 2006), SN 2008D (XRF 080109; A. M. Soderberg et al. 2008) SN 2010bh (GRB/XRF 100316D; Z. Cano et al. 2011; E. F. Olivares et al. 2012), SN 2011kl (GRB 111209A; A. J. Levan et al. 2014; J. Greiner et al. 2015) SN 2013cq (GRB 130427A; D. A. Perley et al. 2014), SN 2016jca (GRB 161219B; Z. Cano et al. 2017), SN 2017iuk (GRB 171205A; L. Izzo et al. 2019), SN 2019oyw (GRB 190829A; Y. D. Hu et al. 2021; J. C. Rastinejad et al. 2024), and SN 2024gsa (EP 240414a; S. Srivastav et al. 2025). For events without high-energy counterparts, we show a subset of Type Ib/c and Ic-BL SNe from the literature (R. J. Foley et al. 2003; M. R. Drout et al. 2011; L. Izzo et al. 2020; A. Y. Q. Ho et al. 2020), which we normalize in time to the peak of SN 2025kg in each respective filter. We show all light curves in the nearest rest-frame filter using their known redshifts (Figure 4).

This comparison (Figure 4) highlights that SN 2025kg's luminosity is comparable to most GRB-SNe, particularly SN 1998bw, and distinct from SNe observed without high-energy counterparts. Among the SNe associated with FXTs, the closest analogs of SN 2025kg are SN 2006aj and SN 2024gsa, the latter of which is also associated with an EP FXT. The optical light curve of SN 2024gsa is marked with a large flare between δt = 1.5–3 days (e.g., S. Srivastav et al. 2025; J. N. D. van Dalen et al. 2025), which we do not observe in early observations of SN 2025kg (R. A. J. Eyles-Ferris et al. 2025).

3.2. SN 2025kg Spectra and Broadened Hα at δt = 42.5 days

We next attempt to compare our spectra of SN 2025kg to past GRB-SNe, FXT-SNe, Type Ic-BL SNe without a high-energy trigger, and AT 2018cow, the latter of which is a benchmark event showing broadened Hα emission (S. J. Prentice et al. 2018; R. Margutti et al. 2019; D. A. Perley et al. 2019). We download spectra from WISeREP (O. Yaron & A. Gal-Yam 2012) of the prototypical GRB-SN, SN 1998bw (F. Patat et al. 2001), three SNe associated with FXTs, SN 2006aj (E. Pian et al. 2006), SN 2008D (M. Modjaz et al. 2006, 2014),

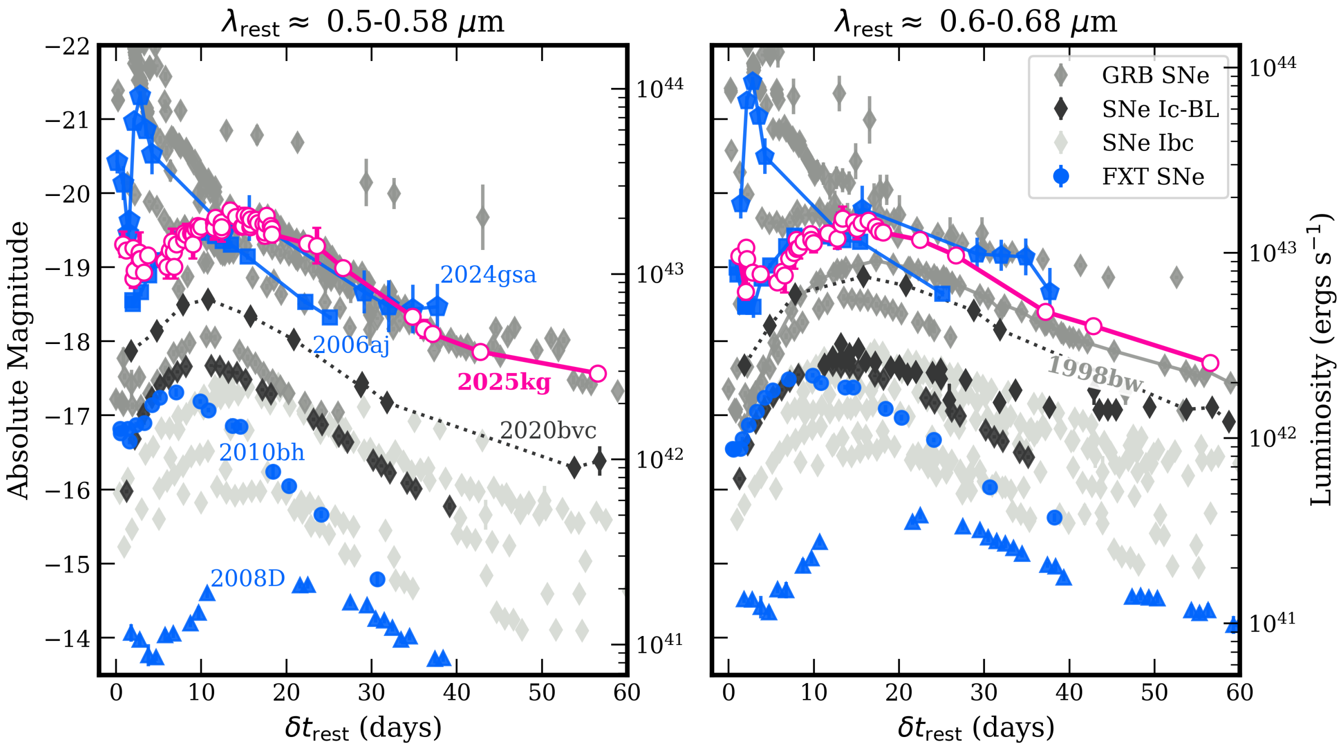

Figure 4. Light-curve comparison of SN 2025kg (pink circles) and SNe associated with FXTs (blue), GRB-SNe (gray diamonds), Type Ic-BL SNe observed without GRB counterparts (dark gray diamonds), and Type Ib/c SNe (light gray diamonds). Observations are corrected for Milky Way extinction (E. F. Schlafly & D. P. Finkbeiner 2011) and presented in the nearest rest-frame band using the event's known redshift. The light curve of SN 2025kg strongly resembles those of SN 1998bw, SN 2006aj, and SN 2024gsa in its peak luminosity and temporal evolution.

and SN 2010bh (F. Bufano et al. 2012), and SN 2020bvc (D. Hiramatsu et al. 2020). Further, we incorporate spectra of the luminous fast blue optical transient, AT 2018cow, in which broadened Hα was prominently observed starting at ≈15 days following the event's detection (e.g., R. Margutti et al. 2019; D. A. Perley et al. 2019; D. Xiang et al. 2021).

In Figure 5 we show the spectra for GRB-SNe and FXT-SNe within a week of the SN peak (δt = 17.5–21.4 days) and the spectrum of SN 2020bvc taken 1.9 days after the explosion (no later spectra are available on WISEReP). Spectra of the Type Ib SN 2008D show prominent He I 4471, 5876, 6678, and 7061 Å absorption lines (M. Modjaz et al. 2009), which we do not observe in SN 2025kg. Considering the remaining spectra, at both epochs, SN 2010bh is less visually comparable to SN 2025kg than SN 2006aj and SN 1998bw, which we attribute in part to its larger ejecta velocities (see Section 3.3; R. Chornock et al. 2010). Similar to their light-curve properties (Section 3.1) SN 1998bw and SN 2006aj are spectroscopically comparable objects to SN 2025kg (Section 2.2). SN 2020bvc also shows a comparable shape to SN 2025kg. We note that SN 2020bvc was also comparable to SN 2025kg in terms of photometric color, blackbody radius, and X-ray properties during the early ($\delta t \lesssim 6$ days) fast-cooling phase, as shown in our companion Letter (R. A. J. Eyles-Ferris et al. 2025).

Turning to the broadened Hα emission, we fit a simple Gaussian profile to the feature (omitting the narrow component using `curvefit`, finding an FWHM value of ∼50 Å. We next compare our SN 2025kg spectrum at δt = 42.5 days to those of SN 1998bw, SN 2010bh, and AT 2018cow at δt = 42.5–48.6 days in the region of Hα (Figure 6). Spectra of SN 2006aj beyond 20 days of the initial high-energy trigger are not available on WISeREP. Compared to the spectrum of SN 2025kg binned at a resolution of 40 Å, the broadened emission feature is stronger and more narrow in AT 2018cow and absent or very weak in SN 2010bh. Though a comparable bump in the spectrum of SN 1998bw is observed, we note that this likely due to two absorption features on either side of Hα. Further, in SN 1998bw the spectral shape in this region is is broadly consistent across several weeks of observations. In contrast, in SN 2025kg the continuum is fairly flat over ∼5700–6000 Å at most epochs, but exhibits broad Hα at one single epoch (Figure 3). Thus, we conclude that absorption features cannot explain the broadened emission feature in SN 2025kg, and that its most likely interpretation is that it arises from H interaction.

Whether this feature is common in FXT-SNe but not GRB-SNe, or if SN 2025kg is an outlier among other FXT-SNe remains to be seen. Indeed, since the H appears only in one spectrum it may be a transient feature that could occur more frequently in other Type Ic-BL SNe but is often missed because it appears only at later times, and is only visible for a short period. One potential explanation for this feature in SN 2025kg is interaction with an extended H shell of circumstellar material (CSM), as was considered for AT 2018cow (R. Margutti et al. 2019; D. A. Perley et al. 2019). However, in AT 2018cow the broadened Hα signature was stronger compared to the continuum, persisted over several weeks, and was generally narrower, whereas in SN 2025kg the feature is weaker and absent in the spectrum at δt = 47.7 days (Figure 2). Alternatively, this could be a signature of a stellar companion, as is observed in a small (1%–5%) fraction of Type Ia SNe (K. Maguire et al. 2016; M. A. Tucker et al. 2020). A larger sample of spectra at $\delta t \gtrsim 30$ days is critical to exploring the presence and temporal

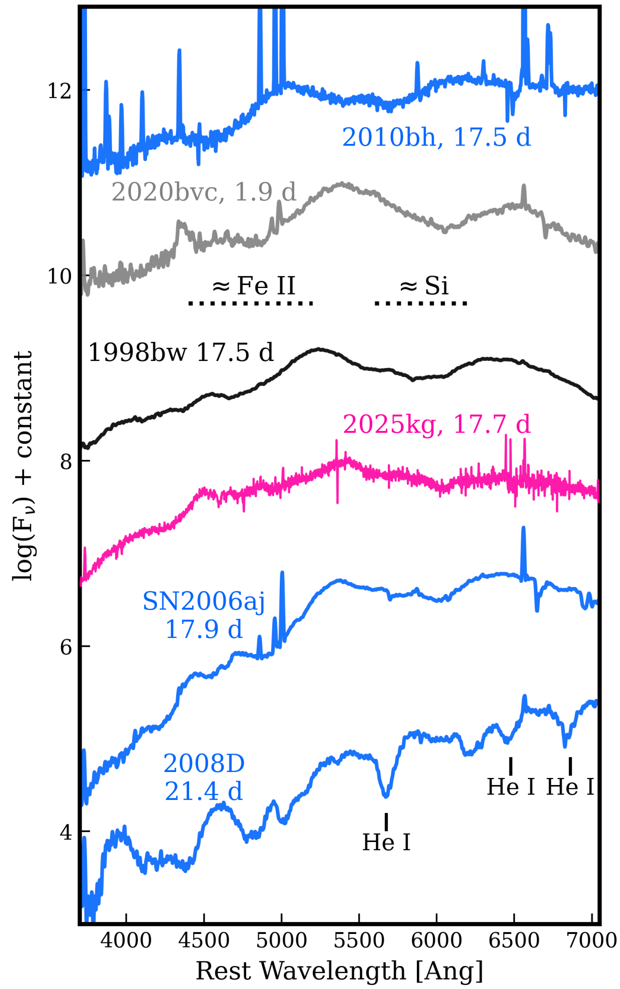

Figure 5. Comparison of SN 2025kg spectra (pink) to SN 1998bw (black; F. Patat et al. 2001), and three SNe associated with FXTs (blue), SN 2006aj (E. Pian et al. 2006), SN 2008D (M. Modjaz et al. 2009, 2014), and SN 2010bh (F. Bufano et al. 2012) around their SNe peak. We also show a spectrum of the Type Ic-BL SN 2020bvc (D. Hiramatsu et al. 2020) taken ∼1.9 days postexplosion. We label the approximate locations of Fe II λ5169 and Si λ6355. Due to its broad-lined features and lack of He lines (labeled in SN 2008D) SN 2025kg is comparable to SN 1998bw and SN 2006aj.

evolution of broadened Hα in future FXT-SNe. We further discuss implications of this feature in Section 5.3.

3.3. Broad-line Velocity Measurements

We compute the ejecta expansion velocity using the Doppler shift of the absorption minima ascribed to Fe II λ5169 and Si λ6355, which are well characterized in GRB-SNe (e.g., R. Chornock et al. 2010; F. Bufano et al. 2012). For each spectrum, we fit the wavelength region around the absorption feature with a linear continuum and Gaussian profile using `scipy.curvefit`, and determine the velocity using the absorption minima's shift relative to the rest-frame wavelength. We show the results from our fitting over time and compare to values for several GRB-SNe and a Type Ic-BL SN (R. Chornock et al. 2010) in Figure 7.

We derive the velocity evolution for both Fe II λ5169 and Si λ6355. Though slight discrepancies between the velocities are present at several epochs, we note that measurements of expansion velocity using different lines are known to produce

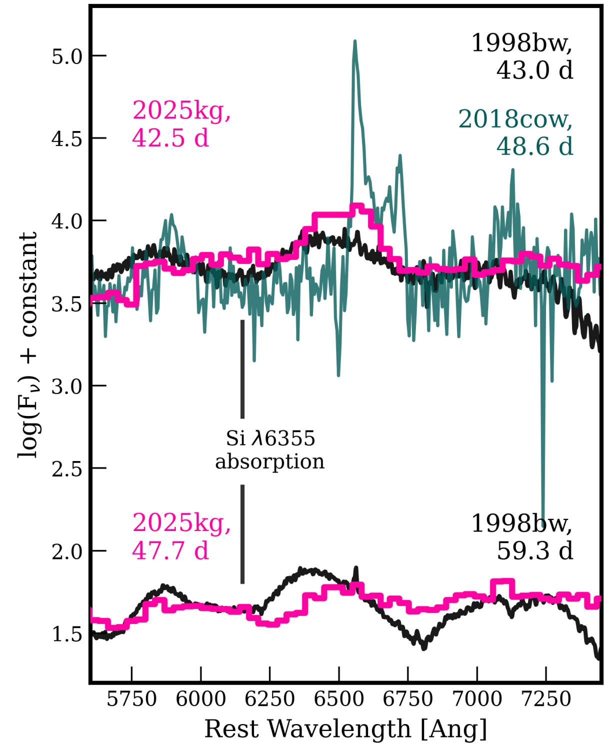

Figure 6. Spectra of SN 2025kg centered around Hα at δt = 42.5 and 47.7 days binned at 40 Å (pink) in which regions affected by the telluric and narrow Hα have been removed. We observe a broadened Hα emission feature in the SN 2025kg Gemini-South/GMOS spectrum at δt = 42.5 days. We observe broadened Hα in the ESO/NTT spectrum of AT 2018cow (green) but not in the Danish/DFOSC spectrum of SN 1998bw (black) at similar epochs.

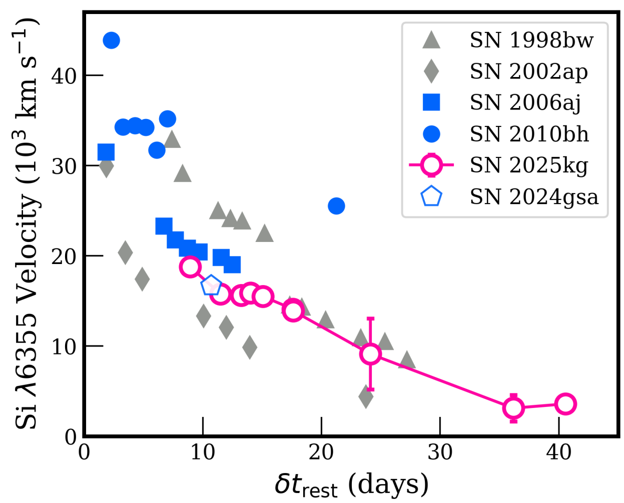

Figure 7. Si λ6355 velocities of SN 2025kg (pink circles) along with literature values for GRB-SNe, FXT-SNe, and Type Ic-BL SN 2002ap (R. Chornock et al. 2010). SN 2025kg is comparable in absorption velocity to SNe 1998bw and 2006aj.

inconsistent values, in part due the locations of each element within different layers of the ejecta (M. Modjaz et al. 2016; G. Finneran & A. Martin-Carrillo 2024). We next compare to the Si λ6355 velocities of SNe 1998bw, 2002ap, 2006aj, and 2010bh (R. Chornock et al. 2010) and the only other confirmed EP SN, SN 2024gsa (EP 240124A; H. Sun et al. 2024; J. N. D. van Dalen et al. 2025), for which one measurement

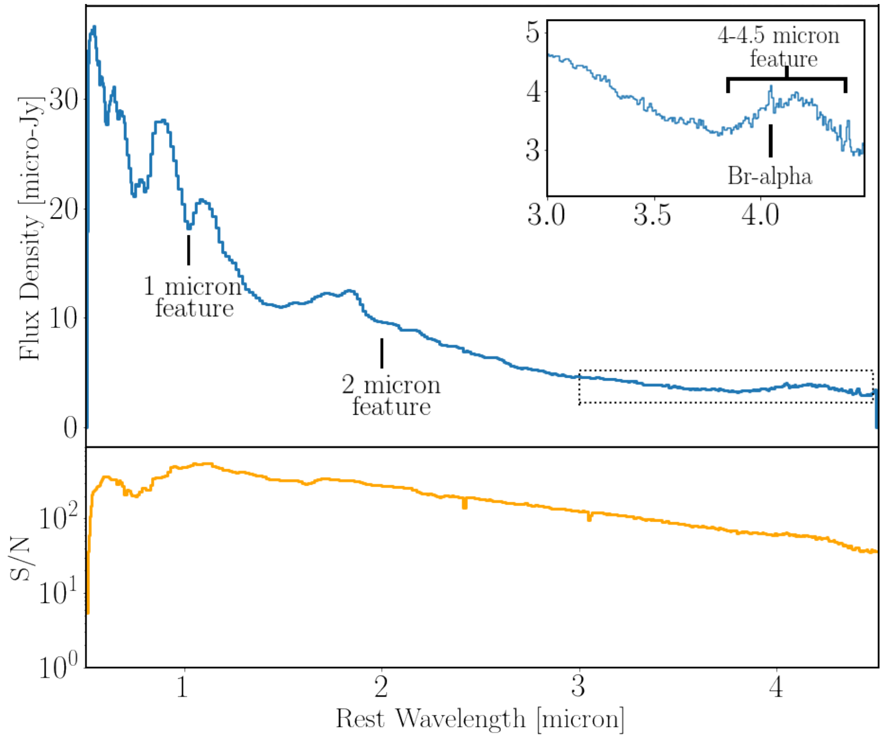

Figure 8. The JWST spectrum of SN 2025kg near maximum light. In the top and bottom panels we show the 1D spectrum and the S/N, respectively. In the top panel, we highlight the three features discussed in detail in Section 3.4 (the 1 μm and 2 μm features) and Section 3.5 (the 4–4.5 μm feature, shown in the inset panel).

at $\delta t \approx 15$ days is available (Figure 7, bottom panel; H. Sun et al. 2024). At this epoch, the expansion velocities of SN 2025kg and SN 2024gsa are comparable. Compared to the wider sample of events, SN 2025kg appears most closely related to SN 2006aj, although the temporal coverage is not equivalent. SN 2025kg has larger measured velocities compared to the Type Ic-BL SN 2002ap and, generally, lower velocities compared to SN 1998bw and SN 2010bh.

3.4. Near-infrared Evidence for Helium

Motivated by questions of the unknown stellar progenitors of FXTs, we next investigate to what degree He is present in the spectra of SN 2025kg. In our optical spectra, we do not observe prominent He I 4471, 5876, 6678, and 7061 Å absorption lines, as were observed in SN 2008D (Figure 5; A. M. Soderberg et al. 2008). However, as He produces stronger signatures in the near-IR compared to the optical, we focus our search on the He I lines 1.0830 μm and 2.0581 μm in the near-IR spectra. He I 1.0830 μm is a prominent feature that dominates the 1 μm region in Type Ib SNe, and may be blended with C I 1.0693 μm and Mg II 1.0927 μm lines in Type Ic/Ic-BL SNe (e.g., M. Shahbandeh et al. 2022; S. Tinyanont et al. 2024). Though it is well established that the He I 1.0830 μm line is a more dominant line compared to He I 2.0581 μm, the redder He I line has a greater offset from other potential absorption features and, thus, may be easier to distinguish as He I (M. Shahbandeh et al. 2022; S. Tinyanont et al. 2024). In the GNIRS spectrum, we do not observe any significant absorption features in the 1 μm regime, though we note that the majority of the spectrum has a low S/N.

Turning to the JWST spectrum, we observe a prominent, broadened absorption feature at $\sim$1 μm and, potentially, a shallower absorption feature at $\sim$2 μm (Figure 8). To investigate the source and significance of these features, we utilize a Bayesian toolkit to jointly model the 1 μm and 2 μm features as blended absorption features from multiple species with Gaussian components (C. Liu et al. 2023).[57] We give the priors for our fits in Appendix A.2. We note that the errors on the velocity found through this method do not encompass the uncertainties in the fit to the continuum. Thus, the true uncertainties are likely larger than those reported here.

First, we test the significance of the possible feature at $\sim$2 μm as, if real, the feature would provide a second observational constraint on the presence of He I. We apply two models and compare their χ^2 and their Bayesian information criterion (BIC). The first model fits the 2 μm region with a linear function, a reasonable approximation for the continuum in the limited wavelength regime, while the second applies a Gaussian to represent an absorption feature. We find that the Gaussian model results in an improvement in χ^2 and BIC of $\sim$3500 compared to the linear fit, suggesting that the 2 μm feature is real.

We next evaluate fits to the 1 μm and 2 μm features for He I, C I, and/or Mg II. The larger width of the 1 μm feature relative to the 2 μm feature (Figure 9) suggests a larger dispersion velocity. In turn, this implies that the 1 μm feature is not due to one element alone and is instead likely a blend of He I, C I, and/or Mg II. Thus, we first fit both features for He I 1.0830 μm and 2.0581 μm, and C I 1.0693 μm and 2.1259 μm (Figure 9). This fit finds He dominates the 2 μm feature and is blended with C I in the 1 μm feature. Both the C I (17,600 $\pm$ 200 km s^{-1}) and He I (14,500 $\pm$ 100 km s^{-1}) expansion velocities are similar to the Si velocities at a similar epoch (Figure 7). A second fit replacing C I with Mg II results in a similar He I velocity and a

[57] https://github.com/slowdivePTG/BayeSpecFit

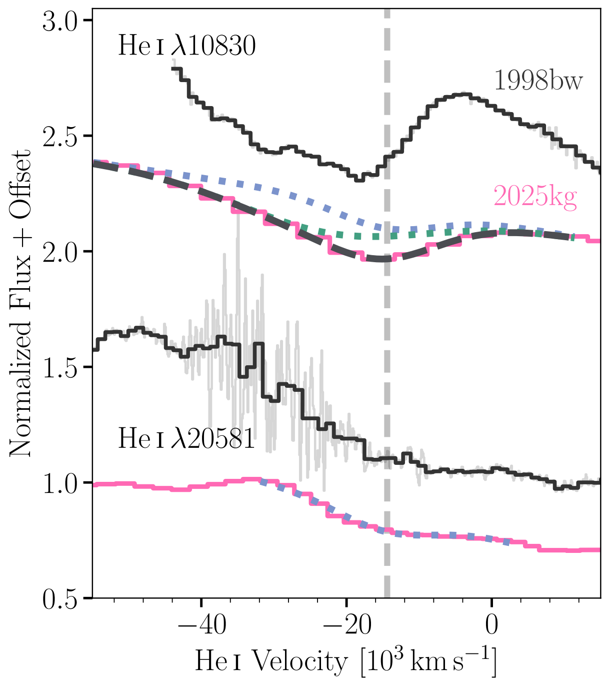

Figure 9. The JWST/NIRSpec spectrum of SN 2025kg (pink) and the near-IR spectrum of SN 1998bw (black; binned to mitigate telluric noise in the spectrum) in velocity space around the 1 μm (upper) and 2 μm (lower) features. We show our combined fit (gray dashed) and individual contributions to the 1 μm feature due to C I (1.0693 μm and 2.1259 μm; dotted turquoise) and He I (λ10830 and λ20587; dotted blue) absorption. We also mark the velocity derived from a single Gaussian fit to the 1 μm feature with a vertical gray line. In the top spectrum, the superposition of the C I and He I absorption provides a strong fit to the observed feature. Our analysis (Section 3.4) shows that a small ($\lesssim$0.5 $M_\odot$) amount of He is likely present in SN 2025kg.

higher Mg II velocity (21,700 ± 100 km s^{-1}). Finally, we explore if the 1 μm and 2 μm features can be explained with only C I and Mg II or a combination of the two (i.e., no He I). We find expansion velocities in the range of 24,000–41,000 km s^{-1}, ≈10,000 km s^{-1} faster than the Si expansion velocities at a similar epoch (Figure 7). This finding implies that the 1 μm and 2 μm features are most reasonably fit with the presence of He I.

The most consistent expansion velocities with optical lines (Section 3.3) are derived from fits to these regions that include some He I. We also note that the best-fit pseudoequivalent width (EW) ratio EW(He I 1.0830 μm)/EW(He I 2.0581 μm) from our first fit is ≈1, in line with predictions for these components (L. B. Lucy 1991), also consistent with the presence of He. Blending of He I and another feature is supported by a higher-resolution near-IR spectrum of SN 1998bw spectrum showing two subfeatures within the 1 μm feature (Figure 9).

We conclude that there is likely a small amount of He in the ejecta of SN 2025kg, though a precise estimate is outside the scope of the current work. Based on the absence of He I lines in the optical (Figures 2 and 5) we place a conservative upper limit on He in the ejecta of $M_{\rm He} \lesssim 0.5\ M_\odot$ (see, e.g., models for Type Ib/c SN optical spectra in L. Dessart et al. 2020, which are independent of engine type). The extent of He mixing in the ejecta may significantly impact the observed signature (e.g., L. Dessart et al. 2020, 2024).

In Figure 9 we show the SN 2025kg JWST spectrum and a near-IR SN 1998bw spectrum (8 days postpeak; F. Patat et al. 2001) in velocity space relative to the He I and Mg II features. Both spectra show evidence for absorption around the 1 μm and 2 μm features, with the 1 μm feature being most prominent. Near-IR spectra of SN 1998bw were taken at 8, 33, and 51 days postpeak, and each shows a prominent feature near 1 μm ascribed to He I (F. Patat et al. 2001), which was not observed in a near-IR spectrum of SN 2010bh (R. Chornock et al. 2010). Further, in the SN 1998bw spectrum at +51 days postpeak F. Patat et al. (2001) also claim the detection of He I 2.0581 μm and state this line is weakly detected in the spectra at +8 and +33 days postpeak (F. Patat et al. 2001). We observe a similar shape at ∼2 μm in the spectra of SN 2025kg and SN 1998bw around peak (Figure 9). Altogether, this comparison demonstrates that small amounts of He are likely common in GRB-SNe and FXT-SNe, but are not typically observed due to a paucity of near-IR spectroscopic coverage.

3.5. 4–4.5 μm Feature

We next turn to the broad emission feature centered at a rest-frame wavelength of ∼4.2 μm in JWST/NIRSpec spectrum taken around SN 2025kg's peak (Figure 8). Here, we discuss several potential explanations for this feature, but ultimately determine that a larger sample of observed events is critical to establishing its origin.

First, we investigate the possibility that this feature is a signature of *r*-process nucleosynthesis. Infrared excesses have been suggested as possible evidence of the *r*-process, which may occur in the accretion disk after the collapse of massive, rapidly rotating stars that are thought to be the progenitors of GRBs and some FXTs (e.g., D. M. Siegel et al. 2019; Y. Zenati et al. 2020). To test this possibility, we explore if the 4.2 μm feature is consistent with a thermal signature. We find that this condition is not satisfied, as the feature is too narrow to be well fit with a Planck function. Further, the peak wavelength implies a temperature of ∼700 K, from which we infer a radius of $\sim 2 \times 10^{16}$ cm to match the luminosity. This would require an average expansion velocity of 0.9*c* over the first two rest-frame weeks, which is incompatible with both observations (Section 3.3) and theoretical expectations.

Second, we consider the possibility that this feature is due to dust. To investigate this, we consider comparable spectroscopic observations of SNe at mid-infrared (mid-IR) wavelengths to investigate their timescales for dust emergence, which are thus far limited in the literature. JWST NIRSpec and MIRI spectroscopic observations of the Type IIP SN 2022acko show no evidence for dust at 50 days following the explosion (M. Shahbandeh et al. 2024). In SN 1987A, near-IR spectra cover the range 1.05–4.1 μm (W. P. S. Meikle et al. 1989). The 4 μm region is dominated by a narrow emission feature that is attributed to Brα ($\lambda_{\rm peak}$ = 4.053 μm). H features are not expected in a Type Ic-BL SN like SN 2025kg, although we note a narrow excess at this wavelength in our spectrum (Figure 8), which may be emission from the underlying host galaxy. In SN 1987A, at around 260 days postpeak a comparable broad underlying feature emerged and was tentatively suggested to be due to an overtone of silicon monoxide (SiO; W. P. S. Meikle et al. 1989). Both of these epochs are significantly later than our JWST spectrum of SN 2025kg, which was taken at ≈15 rest-frame days after the FXT trigger. Additionally, at this point, the ejecta temperature is likely too high for dust molecules to form, supporting that this feature is not SiO. Further, spectral synthesis modeling indicates that the SiO overtone emission emerges at ≳100 days

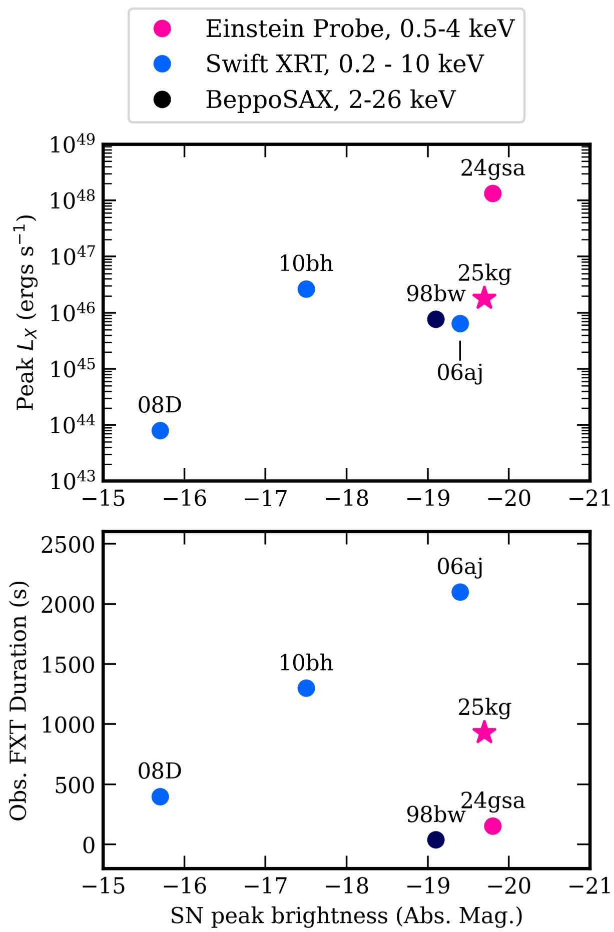

Figure 10. Comparison of the SN peak time and FXT properties of several FXT events with SN counterparts (SNe 1998bw, 2006aj, 2008D, 2010bh, 2024gsa, and 2025kg). EP 250108a/SN 2025kg is marked with a pink star in the first two rows. We caution that the different instruments' bandpasses and slewing strategies impact both the X-ray peak luminosities and durations, making direct comparisons inadvisable. However, the span of several orders of magnitude in some parameters mitigate some of these biases.

following core collapse in Type Ic-BL SNe (S. Liljegren et al. 2023).

Finally, the feature may be the result of nebular Fe lines. This interpretation would require regions of the ejecta to become optically thin, which may be possible with high expansion velocities. Expansion velocities of $\sim$0.1c were inferred at early time in R. A. J. Eyles-Ferris et al. (2025), which may be sufficient to produce this signature. Looking forward, the assembly of a sample of mid-IR spectra of stripped-envelope SNe or other FXTs will be important to understand how ubiquitous this feature is, and shed light on its physical origin.

3.6. Comparison of Supernova and High-energy Properties

In our companion Letter, we show that EP 250108a/SN 2025kg's prompt FXT, early ($\delta t \lesssim 6$ days) optical light curve, and radio upper limits are consistent with a trapped or weak jet from a collapsar (R. A. J. Eyles-Ferris et al. 2025). Motivated to explore if this event is a typical FXT-SN, we consider any potential correlations between the high-energy and SN properties of FXTs (Figure 10).

In addition to EP 250108a/SN 2025kg, we include the events SNe 1998bw, 2006aj, 2008D, 2010bh, and 2024gsa in this comparison. We utilize the prompt X-ray (2–26 keV) emission of SN 1998bw detected by BeppoSAX (T. J. Galama et al. 1998; E. Pian et al. 2000), X-ray detections by Swift-XRT of SN 2006aj, SN 2008D, and SN 2010bh pulled from UKSSDC (P. A. Evans et al. 2007, 2009), and the prompt X-ray emission of SN 2024gsa and SN 2025kg observed by EP (H. Sun et al. 2024; W. X. Li et al. 2025b). We caution that these properties are drawn from a variety of instruments, each with different energy ranges and slewing strategies. However, we note that these comparisons span several orders of magnitude, mitigating some biases. We mark the different instruments in Figure 10. For SN properties, we incorporate SN peak magnitudes derived from the light curves presented in Sections 3.1 and Si λ6355 velocities presented in Section 3.3.

Figure 10 highlights that SN 2025 kg, SN 1998bw, and SN 2006aj occupy a similar region in the parameter space of peak SN and peak X-ray luminosity (see also Figure 13 of R. A. J. Eyles-Ferris et al. 2025). We observe a potential trend in these properties for the objects outside of this cluster, though a significantly larger sample is needed to test this trend further. In terms of duration, the Swift events show a potential trend between SN peak brightness and observed FXT duration. We do not observe any correlations between the remaining events.

4. Radioactive Decay Supernova Modeling

With this extensive data set, we are motivated to constrain the physical properties of SN 2025kg, which enable comparisons to previous SNe and possible properties of the progenitor. Thus, we fit the light curve for SN 2025kg using Redback (N. Sarin et al. 2024). We fit the light curve using two models: first, a one-zone "Arnett" model (W. D. Arnett 1982) and second, a model that accounts for mixing of ^{56}Ni into the outer ejecta.

For both models, we fit the entire light curve at $\delta t \gtrsim 6.5$ days assuming a Gaussian likelihood. For each photometric point, we include a systematic error of 0.15 mag added in quadrature to the statistical errors to capture any discrepancies caused by differences in photometric reduction, filter transmission curves, or in the model itself. We explore the model parameter space using Bayesian Inference via the PyMultiNest nested sampler (J. Buchner et al. 2014) through the Bilby library (G. Ashton et al. 2019).

4.1. One-zone Model

We begin with a one-zone "Arnett" model that assumes a one-zone, homologously expanding ejecta powered by a centrally located heating term (i.e., the ^{56}Ni) with a gray ejecta opacity that is constant in time. This model is commonly invoked to describe the physical properties of SNe. We consider seven model parameters for the one-zone model here: ejecta mass, $M_{\rm ej}$; fraction of ^{56}Ni in the ejecta, $f_{\rm Ni}$; ejecta velocity, $v_{\rm ej}$; gray opacity, κ; γ-ray opacity, κ_γ; temperature at which the photosphere begins to recede, $T_{\rm floor}$; and host extinction in magnitude, A_V. For the final parameter, we assume a standard Fitzpatrick extinction law with an $R_V = 3.1$ (E. L. Fitzpatrick 1999). We use broad uninformative priors on each parameter.

Our model provides a strong fit to the data. Our fits with this model are shown in Figure 1 highlighting broad agreement with the data. We infer $1.4 \pm 0.15\ M_{\odot}$ of ejecta with a ^{56}Ni mass of $0.6 \pm 0.1\ M_{\odot}$ and an initial ejecta velocity of $19{,}000 \pm 700$ km s^{-1}. All uncertainties are at the 68% credible interval for the 1D marginalized posterior. Our estimate of ejecta mass and energy is consistent with median values inferred from Type Ic-BL SNe (e.g., F. Taddia et al. 2019; Ó. Rodríguez et al. 2023; G. P. Srinivasaragavan et al. 2024) using a similar model. However, our estimate of the ^{56}Ni is marginally inconsistent with the Type Ic-BL SNe medial values of F. Taddia et al. (2019; at 1σ), which could be due to differences in assumptions about γ-ray opacities or hinting toward a limitation with the one-zone model. We note that our analysis here is based on the photometry, while past works have directly fit a reconstructed bolometric luminosity, which could also explain the discrepancy.

4.2. Caveats to the One-zone Model

There are clear limitations with the one-zone model in its assumption of a centrally located ^{56}Ni and constant opacity. In reality, the opacity is almost certainly not gray or constant with time (e.g., A. E. Niblett et al. 2025) and ^{56}Ni is likely mixed out to large radii due to Rayleigh–Taylor or jet-driven instabilities (e.g., D. K. Khatami & D. N. Kasen 2019; M. Reichert et al. 2023). The latter effect significantly impacts the overall bolometric light curve. In particular, the classical "Arnett-like" one-zone model often overpredicts the quantity of ^{56}Ni compared to models with mixing (e.g., M. C. Bersten et al. 2014) for two reasons. First, the central heating term is forced to overcome adiabatic losses compared to heating from ejecta at larger radii. Second, energy through heating has to diffuse through more ejecta. Therefore, our ^{56}Ni mass measurement above is likely an overestimate. Additional luminosity in the form of a central engine could also provide an alternative path to powering the light curve, which would naturally reduce the quantity of ^{56}Ni.

In Appendix A.1 we present an alternate model in which ^{56}Ni is mixed with the outer SN layers, resulting in a lower best-fit value for the ^{56}Ni mass ($0.2\ M_{\odot}$). Though this model offers several advantages compared to the one described in Section 4, there are still uncertainties, such as the assumed mass profile, therefore, we conservatively use the ^{56}Ni estimate from both models. These masses and mixing provide some strong hints into the progenitor, as we discuss in Section 5.

Finally, we have assumed that the peak emission is powered entirely by ^{56}Ni decay. Shock heating can contribute to the peak emission, reducing the requirements on the ^{56}Ni mass (A. E. Niblett et al. 2025).

5. Discussion

Our analysis of the light curves and spectra of SN 2025kg place strong constraints on the nature of the progenitor. In our companion Letter (R. A. J. Eyles-Ferris et al. 2025) we argue that the engine behind this transient is jet driven, supported by shock breakout model fits to the prompt X-ray emission, upper limits on radio emission, and the blue and rapidly fading light curve prior to the onset of the SN. In this section, we combine the inferences of both Letters to discuss constraints on the progenitor and implications for the population of FXTs from collapsars.

5.1. Constraints on the Zero-age Main-sequence Mass of the Progenitor

Here, we determine the ZAMS mass of the progenitor by combining the inferred masses on the ejecta yield, the ^{56}Ni yield (which dictates the disk mass), and the compact remnant mass. We note that the ^{56}Ni mass may be overestimated due to luminosity contributions from additional sources, but do not anticipate this significantly impacts our order-of-magnitude estimates. To do this, we set the mass of the star at explosion to the C/O core mass as SN 2025kg shows evidence for stripping of its H and most of its He layers; Section 2.2. We assume that the C/O core mass will be equivalent to the summation of the ejecta mass, the disk mass, and the compact object remnant mass. For the first component, we use the results from our light-curve fits, which indicate a total ejecta mass of 0.8–1.4 $M_{\odot}$ with a ^{56}Ni mass of 0.2–0.6 $M_{\odot}$ in SN 2025kg (Section 4). We explore two scenarios to determine the latter two components: a black hole accretion disk jet model and a model invoking a neutron star accretion disk. If the remnant is a black hole, we assume the accretion disk forms around a 3–5 $M_{\odot}$ black hole. If it is a neutron star, we assume an initial remnant mass of 1.4 $M_{\odot}$.

The large amount of ^{56}Ni ejecta mass required to explain the SN light-curve peak (Section 4) indicates that a considerable mass must be processed through an accretion disk. In a jet-driven explosion, the ^{56}Ni is primarily produced in the high-temperature disk and ejected through a disk wind (R. Surman et al. 2006). Typically models predict that ∼20% of the disk is lost through a wind (e.g., R. Aktar et al. 2017; D. M. Siegel & B. D. Metzger 2017). This means that the mass that flows into the disk must be greater than 5 times that of the ^{56}Ni ejecta mass. To eject 0.2–0.6 $M_{\odot}$ of ^{56}Ni, roughly 1–3 $M_{\odot}$ would have to be processed through a disk. Combined with the nonnickel ejecta mass and the compact remnant mass, this corresponds to a C/O core of ∼3.0–5.2 $M_{\odot}$ for a neutron star accretion disk model or ∼4.6–8.8 $M_{\odot}$ for a black hole accretion disk model. Using the C/O star masses from low-metallicity stars simulated by S. E. Woosley et al. (2002), the C/O core masses correspond to a ZAMS progenitor mass of 15–21 $M_{\odot}$ if the compact remnant is a neutron star or 19–30 $M_{\odot}$ if the compact remnant is a black hole. These mass ranges are consistent with our current expectations for the progenitors of neutron stars and black holes, respectively (C. L. Fryer 1999). The uncertainty in the ^{56}Ni mass dominates the wide range of our predicted progenitor masses. A late-time observation of the light curve will help constrain the ^{56}Ni mass and place stronger constraints on the progenitor's ZAMS mass. Finally, we note that our above estimates are based on single star models with a fixed set of parameters for stellar evolution (e.g., mixing; S. E. Woosley et al. 2002). Models that include the effects of binary mass transfer and ejection are likely to alter or broaden the predicted range of progenitors. However, these results provide a first pass of the stellar conditions.

5.2. Constraints on an He Shell

In our companion Letter (R. A. J. Eyles-Ferris et al. 2025) we find that the early optical light curve of the counterpart of EP 250108a ($\delta t \lesssim 6$ days) is marginally consistent with interaction of a 0.2–0.9 $M_{\odot}$ shell at a distance of 7×10^{14} cm. While we note that the preferred model to explain the early light curve is a shocked cocoon from a jet (R. A. J. Eyles-Ferris et al. 2025), here we briefly consider the implications of this alternate possibility for a shell around the progenitor of EP 250108a/SN 2025kg from our observations. This distance is consistent with being produced by a common envelope mass ejection of an He shell, and just below the lower radii predicted for He shell mass ejection from a common envelope if it occurs at C ignition (C. L. Fryer et al. 2025). This distance is also consistent with an He merger event (C. L. Fryer & S. E. Woosley 1998; A. Grichener 2025).

Using the He shell models of S. E. Woosley et al. (2002), we predict a large amount of He in this shell ($>1\ M_{\odot}$). This He shell will be swept up into the ejecta and behind the photosphere at the time of our optical spectra. Notably, this predicted shell mass is inconsistent with both the upper limit on the He mass of $<0.5\ M_{\odot}$ from the optical spectra (L. Dessart et al. 2020; Section 3.4) and the mass of the shell derived in our companion Letter (R. A. J. Eyles-Ferris et al. 2025). This He shell mass could be reduced if significant Wolf–Rayet mass loss occurs prior to the final mass ejection episode that produces the shell at 7×10^{14} cm. Alternatively, enhanced mixing (e.g., L. H. Frey et al. 2013) could reduce the size of the He shell. In conclusion, for our models to fit the data presented in R. A. J. Eyles-Ferris et al. (2025) and this work, either considerable wind mass loss or stellar mixing is required.

5.3. Implications of the Hydrogen Observed at $\delta t = 42.5$ days

In Section 2.2 we show that broadened Hα is observed at $\delta t = 42.5$ days, or when the shock reaches $\sim 10^{16}$ cm. Similarly, the Type I superluminous SN iPTF13ehe showed a similar late-time Hα feature initially observed in spectra at +251 days from peak light, which was interpreted as coming from a detached shell of H around 10^{16} cm from the progenitor star (L. Yan et al. 2017).

Here, we briefly consider several potential explanations for this feature. We find it unlikely that the H is due to the progenitor star's wind, as models robustly predict that a Wolf–Rayet wind would evacuate the H in a region with radial extent of 0.1–1 pc (R. Weaver et al. 1977).

One potential explanation could be that the Hα signature could be produced through interaction with a companion star. However, such a wide separation would argue that this companion star had no impact on the stellar evolution of the collapsing star. To ensure that the SN blast wave sweeps up enough H to produce the Hα line, this companion would have to be evolved, either in a giant or supergiant phase (R. Hirai et al. 2018, 2020; R. Hirai 2023). Since we are likely to require a close binary to explain the rotation and loss of the He shell, this would then imply that the progenitor of SN 2025kg is in a triple system. However, we disfavor the triple companion explanation due the giant or supergiant phase requirement and the temporal likelihood of being in this phase. Furthermore, based on hydrodynamical simulations, material stripped from a companion by the SN ejecta will have velocities of order the escape velocity from the companion, too low to match the observed H broadening.

Alternatively, the Hα signature could be due to clumps of H-rich material surrounding the SN produced by an asymmetric common envelope mass ejection phase (e.g., E. Quataert et al. 2016; C. L. Fryer et al. 2020, 2023). These clumps could be sufficiently dense that they could persist despite the strong Wolf–Rayet wind (e.g., S. P. Owocki & G. B. Rybicki 1984; J. Puls et al. 2008). Post-SN binary interactions that cause ongoing energy injection through feedback from H-rich material accretion or through magnetar winds ablating an H-rich companion (E.g., J.-P. Zhu et al. 2024) could produce a similar dense cloud. We favor this explanation for the Hα signature observed at $\delta t = 42.5$ days.

5.4. A Growing Population of Fast X-Ray Transient Supernovae and Connections to γ-Ray Burst Supernovae and Type Ic-BL Supernovae

Early works on XRF/FXTs with SNe found that the volumetric rates of such events would be at least an order of magnitude higher than those of collapsar GRBs (A. M. Soderberg et al. 2008). EP 250108a/SN 2025kg joins a population of three FXT-SNe (EP 240414a/SN 2024gsa and EP 250304a; H. Sun et al. 2024; L. Izzo et al. 2025; J. N. D. van Dalen et al. 2025) discovered in just the first year of EP operations. Of those with published SNe light curves and spectra (EP 240414a/SN 2024gsa and now EP 250108a/SN 2025kg) these events are comparable in their peak optical luminosities, optical spectra, and Si λ6355 absorption velocities (Sections 3.1–3.3) to GRB-SNe and the XRF/FXT 060218/SN 2006aj. Further, in Section 3.6, we demonstrated that the peak X-ray luminosities of GRB 980425, XRF/FXT 060218, and EP 250108a are also comparable. Taken together, these support a causal link between the progenitors and mechanisms driving GRBs and FXTs with SNe.

The three recent EP FXT detections and the rates of GRB-SNe discovered over the last 20 yr ($\lesssim$1 per year; e.g., M. G. Dainotti et al. 2022) support earlier calculations (A. M. Soderberg et al. 2008) that FXT-SNe are significantly more common than GRB-SNe. While a robust calculation of the relative rates of FXT-SNe and GRB-SNe is outside the scope of this work, we note that the three FXT-SNe discovered in the first year of EP operations were at $z = 0.40$, 0.17, and 0.20 and detected by an instrument covering $\sim$9% of the sky. From this, we derive an estimate of the intrinsic volumetric rates of at least several tens of cubic gigaparsecs per year, 1–2 orders of magnitude larger than the rate of on-axis luminous GRBs (H. Sun et al. 2015).

In our companion Letter (R. A. J. Eyles-Ferris et al. 2025) we demonstrate that EP 250108a/SN 2025kg is consistent with being driven by a collapsar-powered jet that either fails to break out of a dense CSM or has an energy weaker than $\sim 10^{50}$–10^{51} erg. Taken together with the rates, this indicates that trapped or weak jets are more common than the successful jets that produce GRBs. The lack of radio and X-ray detections at later times following EP 250108a/SN 2025kg (R. A. J. Eyles-Ferris et al. 2025) implies that observing any relativistic material may be challenging from these FXT-producing jets, in keeping with late-time radio surveys of Type Ic-BL SNe observed without high-energy counterparts (e.g., A. Corsi et al. 2016). Zooming out, it is likely that FXT-producing, "trapped" jets accompany a substantially larger fraction of Type Ic-BL SNe than those with successful jets and GRBs, representing at least a few percent of the Type Ic-BL SNe population.

Finally, we note that the SNe of two past FXT events, SN 2008D and SN 2010bh, are $\sim$5–100 times less luminous than FXT-SNe 2006aj, 2024gsa, and 2025kg, as well as GRB-SNe, and, in the former case, show prominent He absorption (Figure 5; A. M. Soderberg et al. 2008; M. Modjaz et al. 2009). The lower optical luminosities of these SNe are echoed in the lower peak X-ray luminosities of their FXTs (Figure 10). Future EP detections of FXT-SNe will reveal both the rates of such events and the full span in stellar progenitors of FXT-SNe.

6. Conclusion

Along with our companion Letter (R. A. J. Eyles-Ferris et al. 2025), we have presented the most detailed data set to date of an SN accompanying an EP FXT. Our main conclusions are as follows.

1. Optical spectra of SN 2025kg are characterized by broad absorption features due to Fe II λ5169 and Si λ6355 and do not show obvious emission due to He I, leading to a Type Ic-BL classification.
2. SN 2025kg is a close analog of GRB-SNe, particularly SN 1998bw, and the FXT-SNe SN 2006aj and SN 2024gsa, in terms of its peak luminosity, expansion velocities, and spectral evolution. We also find a strong match between SN 2025kg and the Type Ic-BL SN 2020bvc, in keeping with comparisons to the early light curve (R. A. J. Eyles-Ferris et al. 2025).
3. We observe absorption features $\sim$1 μm and 2 μm in the JWST spectrum taken around maximum light, and find that they are well fit with a combination of He I and C I. From optical spectra, we conservatively conclude that the mass of He in the ejecta is $\lesssim$0.5 $M_\odot$.
4. We observe a broad feature at 4–4.5 μm in the JWST spectrum. We investigate several explanations for this feature, including thermal emission due to *r*-process nucleosynthesis, nebular Fe lines, and He emission, but cannot definitively identify its origin with present information.
5. We fit SN 2025kg with a one-zone radioactive decay model and a model that accounts for mixing of ^{56}Ni into the outer SN ejecta. We derive a range in the ^{56}Ni mass of $0.2-0.6$ $M_\odot$.
6. Together, observations presented in our companion Letter (R. A. J. Eyles-Ferris et al. 2025) and this work favor a ZAMS progenitor mass for EP 250108a/SN 2025kg of 15–21 $M_\odot$ or 21–30 $M_\odot$ if the compact remnant is a neutron star or black hole, respectively. It is plausible that the progenitor was surrounded by an He shell ejected during a common envelope episode, and either H-rich clumps due to a prior, asymmetric common envelope ejection or a giant/supergiant tertiary stellar companion.
7. Our analysis supports a causal link between GRB-SNe and FXT-SNe, in which GRBs are produced by successful jets and FXT-SNe are produced by trapped or weak jets. Thus far, the rate of SN detections following EP FXTs indicates that trapped or weak jets are substantially more common than successful (GRB) jets.

EP 250108a is only the second EP transient with an observed SN counterpart to date. Our detailed observational study of SN 2025kg has revealed both similarities with previous FXT and GRB-SNe, and unexpected signals, including H at 42.5 days and the broad 4–4.5 μm feature, which cannot be fully accounted for with current models. Looking forward, the opportunities for detailed observational studies to shed light on the stellar progenitors of FXTs and their catastrophic explosions are only increasing with the continued operations of EP and coordinated rapid follow-up efforts.

Acknowledgments

We dedicate this work to the memory of Alicia M. Soderberg, a pioneer in the study of XRFs and FXTs.

We are deeply grateful to Tom Marsh for developing the MOLLY software, one of his many contributions to advancing the field of compact objects. We thank Jennifer Andrews, the T-80 South technical team, and others for their support during observations.

J.C.R. acknowledges support from the Northwestern Presidential Fellowship. P.G.J., J.N.D.D., J.S.S., J.Q.V., and A.P.C.H. are supported by the European Union (ERC, Starstruck, 101095973). Views and opinions expressed are however those of the author(s) only and do not necessarily reflect those of the European Union or the European Research Council Executive Agency. Neither the European Union nor the granting authority can be held responsible for them. N.S. acknowledges support from the Knut and Alice Wallenberg Foundation through the "Gravity Meets Light" project and by and by the research environment grant "Gravitational Radiation and Electromagnetic Astrophysical Transients" (GREAT) funded by the Swedish Research Council (VR) under Dnr 2016-06012. B.P.G acknowledges support from STFC grant No. ST/Y002253/1 and The Leverhulme Trust grant No. RPG-2024-117 C.D.K. gratefully acknowledges support from the NSF through AST-2432037, the HST Guest Observer Program through HST-SNAP-17070 and HST-GO-17706, and from JWST Archival Research through JWST-AR-6241 and JWST-AR-5441. W.F. gratefully acknowledges support by the David and Lucile Packard Foundation, the Alfred P. Sloan Foundation, and the Research Corporation for Science Advancement through Cottrell Scholar Award 28284. P.O.'B. acknowledges support from the UKRI grant ST/W000857/1. The work by C.L.F. was supported by the US Department of Energy through the Los Alamos National Laboratory. Los Alamos National Laboratory is operated by Triad National Security, LLC, for the National Nuclear Security Administration of U.S. Department of Energy (Contract No. 89233218CNA000001). W.J-G. is supported by NASA through the NASA Hubble Fellowship grant HSTHF2-51558.001-A awarded by the Space Telescope Science Institute, which is operated by the Association of Universities for Research in Astronomy, Inc., for NASA, under contract NAS 5-26555. L.M.R acknowledges support from NSF grants AST-1911140, AST-1910471, and AST-2206490. S.Y. acknowledges the funding from the National Natural Science Foundation of China under grant No. 12303046 and from the Startup Research Fund of Henan Academy of Sciences, grant No. 241841217. A.A.C. acknowledges support through the European Space Agency (ESA) research fellowship program. C.R.B. acknowledges the financial support from CNPq (316072/2021-4), from FAPERJ (grants 201.456/2022 and 210.330/2022), and FINEP contract 01.22.0505.00 (ref. 1891/22). D.M.S. and M.A.P.T. acknowledge support by the Spanish Ministry of Science via the Plan de Generacion de conocimiento PID2020-120323GB-I00. D.M.S. also acknowledges support via a Ramon y Cajal Fellowship RYC2023-044941. M.N. is supported by the European Research Council (ERC) under the European

Union's Horizon 2020 research and innovation program (grant agreement No. 948381). R.G. was sponsored by the National Aeronautics and Space Administration (NASA) through a contract with ORAU. The views and conclusions contained in this document are those of the authors and should not be interpreted as representing the official policies, either expressed or implied, of the National Aeronautics and Space Administration (NASA) or the U.S. Government. The U.S. Government is authorized to reproduce and distribute reprints for Government purposes notwithstanding any copyright notation herein. S.J.S., J.G., S.S., and K.S. acknowledge funding from STFC grant ST/Y001605/1, a Royal Society Research Professorship, and the Hintze Charitable Foundation. C.J.N. acknowledges support from the Science and Technology Facilities Council (grant No. ST/Y000544/1) and from the Leverhulme Trust (grant No. RPG-2021-380). A.A. acknowledges the Yushan Young Fellow Program by the Ministry of Education, Taiwan for the financial support (MOE-111-YSFMS-0008-001-P1). T.-W.C. acknowledges the Yushan Fellow Program by the Ministry of Education, Taiwan for financial support (MOE-111-YSFMS-0008-001-P1). C.L. is supported by DOE award #DE-SC0025599. A.R.E. is supported by the European Space Agency (ESA) Research Fellowship.

Observations reported here were obtained at the MMT Observatory, a joint facility of the University of Arizona and the Smithsonian Institution. MMT Observatory access was supported by Northwestern University and the Center for Interdisciplinary Exploration and Research in Astrophysics (CIERA).

Based on observations obtained at the international Gemini Observatory (Program IDs GN-2024B-Q-131, GN-2024B-Q-107, GS-2024B-Q-105, and GS-2025A-Q-107), a program of NOIRLab, which is managed by the Association of Universities for Research in Astronomy (AURA) under a cooperative agreement with the National Science Foundation on behalf of the Gemini Observatory partnership: the National Science Foundation (United States), National Research Council (Canada), Agencia Nacional de Investigación y Desarrollo (Chile), Ministerio de Ciencia, Tecnología e Innovación (Argentina), Ministério da Ciência, Tecnologia, Inovações e Comunicações (Brazil), and Korea Astronomy and Space Science Institute (Republic of Korea). Data were processed using the Gemini DRAGONS (Data Reduction for Astronomy from Gemini Observatory North and South) package.

This work is based in part on observations made with the NASA/ESA/CSA James Webb Space Telescope. The data were obtained from the Mikulski Archive for Space Telescopes at the Space Telescope Science Institute, which is operated by the Association of Universities for Research in Astronomy, Inc., under NASA contract NAS 5-03127 for JWST. These observations are associated with program #6133. The observation analyzed in this work can be accessed via DOI: 10.17909/a0xj-1h19.

Data for this Letter have in part been obtained under the International Time Programme of the CCI (International Scientific Committee of the Observatorios de Canarias of the IAC) under programm ID ITP24 (PI: Jonker) with the NOT and GTC operated on the island of La Palma by the Roque de los Muchachos. Observations have been made in part with the ALFOSC instrument, which is provided by the Instituto de Astrofisica de Andalucia (IAA) under a joint agreement with the University of Copenhagen and the Nordic Optical Telescope, owned in collaboration by the University of Turku and Aarhus University, and operated jointly by Aarhus University, the University of Turku and the University of Oslo, representing Denmark, Finland and Norway, the University of Iceland, and Stockholm University at the Observatorio del Roque de los Muchachos, La Palma, Spain, of the Instituto de Astrofisica de Canarias.

This publication has made use of data collected at Lulin Observatory, partly supported by MoST grant 109-2112-M-008-001 and TAOVA with NSTC grant 113-2740-M-008-005.

Based on observations obtained with MegaPrime/MegaCam, a joint project of CFHT and CEA/DAPNIA, at the Canada–France–Hawaii Telescope (CFHT), which is operated by the National Research Council (NRC) of Canada, the Institut National des Science de l'Univers of the Centre National de la Recherche Scientifique (CNRS) of France, and the University of Hawai'i. The observations at the Canada–France–Hawaii Telescope were performed with care and respect from the summit of Maunakea, which is a significant cultural and historic site.

Based on observations with the BlackGEM telescope array. The BlackGEM telescope array is built and run by a consortium consisting of Radboud University, the Netherlands Research School for Astronomy (NOVA), and KU Leuven with additional support from Armagh Observatory and Planetarium, Durham University, Hamburg Observatory, Hebrew University, Las Cumbres Observatory, Tel Aviv University, Texas Tech University, Technical University of Denmark, University of California Davis, the University of Barcelona, the University of Manchester, University of Potsdam, the University of Valparaiso, the University of Warwick, and Weizmann Institute of science. BlackGEM is hosted and supported by ESO at La Silla.

Pan-STARRS is primarily funded to search for near-Earth asteroids through NASA grants NNX08AR22G and NNX14AM74G. The Pan-STARRS science products for transient follow-up are made possible through the contributions of the University of Hawaii Institute for Astronomy and Queen's University Belfast.

This work has made use of data from the Asteroid Terrestrial-impact Last Alert System (ATLAS) project. The Asteroid Terrestrial-impact Last Alert System (ATLAS) project is primarily funded to search for near-earth asteroids through NASA grants NN12AR55G, 80NSSC18K0284, and 80NSSC18K1575; by-products of the NEO search include images and catalogs from the survey area. This work was partially funded by Kepler/K2 grant J1944/80NSSC19K0112, HST-GO-15889, and STFC grants ST/T000198/1 and ST/S006109/1. The ATLAS science products have been made possible through the contributions of the University of Hawaii Institute for Astronomy, the Queen's University Belfast, the Space Telescope Science Institute, the South African Astronomical Observatory, and The Millennium Institute of Astrophysics (MAS), Chile.

The Legacy Surveys consist of three individual and complementary projects: the Dark Energy Camera Legacy Survey (DECaLS; Proposal ID #2014B-0404; PIs: David Schlegel and Arjun Dey), the Beijing-Arizona Sky Survey (BASS; NOAO Prop. ID #2015A-0801; PIs: Zhou Xu and Xiaohui Fan), and the Mayall z-band Legacy Survey (MzLS; Prop. ID #2016A-0453; PI: Arjun Dey). DECaLS, BASS, and MzLS together include data obtained, respectively, at the Blanco telescope, Cerro Tololo Inter-American Observatory, NSF's NOIRLab; the Bok telescope, Steward Observatory, University of Arizona; and the Mayall telescope, Kitt Peak National Observatory, NOIRLab. Pipeline processing and analyses of the data were supported by NOIRLab and the Lawrence Berkeley National Laboratory (LBNL). The Legacy Surveys project is honored to be permitted to conduct astronomical research on Iolkam Duág (Kitt Peak), a mountain with particular significance to the Tohono Oódham Nation.

Appendix

A.1. Nickel Mixing Model

To better ascertain the quantity ^{56}Ni and to also explore the impact of mixing on our light-curve fits and estimated parameters, we also fit a ^{56}Ni-mixing model. We outline the details of this model below, but detailed derivations and comparison to the one-zone model will be presented in a forthcoming publication (N. Sarin et al. 2025, in preparation). This derivation is largely inspired by the kilonova model outlined in B. D. Metzger (2019). We begin by assuming a power-law distribution of masses under the assumption of homologous expansion:

$$M_i = M_*(v_i/v_0)^{-\beta}, \tag{A1}$$

where M_* is an arbitrary coefficient such that the sum of all layers is the total ejecta mass, M, v_0 is the minimum velocity of the outflow, and M_i describes the mass in each "layer." The number of layers is arbitrary, provided that they are sufficiently thin to accurately capture the dynamical evolution of the ejecta. A better description of SN ejecta is likely a broken power law (e.g., C. D. Matzner & C. F. McKee 1999). However, the deviations in light curve for different density profiles are smaller than the impact of mixing and other uncertain physics such as γ-ray leakage (e.g., J. Sollerman et al. 1998). The thermal energy of each layer evolves following the first law of thermodynamics:

$$\frac{dE_i}{dt} = \dot{Q}_i - \frac{E_i}{R_i}\frac{dR_i}{dt} - L_i, \tag{A2}$$

where $\dot{Q}_i$ describes the energy input into each layer from radioactive decay, the second term on the right-hand-side describes losses due to PdV expansion, and L_i describes radiative losses from each layer, which needs to account for energy losses due to the light-crossing time (e.g., B. D. Metzger 2019). These equations can be numerically solved while distributing the total ^{56}Ni into layers (following the same distribution as the original mass distribution) up to a certain mass layer set by an additional parameter $f_{\rm mix}$ to capture nickel mixing. The photospheric radius is set as the radius of the mass shell at which $\tau = 1$, which starts to recede back into the ejecta when the temperature drops below $T_{\rm floor}$. We further improve the physics of the model by incorporating a temperature-dependent opacity following

$$\kappa_{\rm eff} = \kappa_{\rm min} + 0.5(\kappa_{\rm max} - \kappa_{\rm min}) \times \left(1 + \tanh\left(\frac{T - T_{\rm floor}}{\Delta T}\right)\right), \tag{A3}$$

where $\kappa_{\rm eff}$ is the effective opacity, which smoothly transitions from the maximum opacity, $\kappa_{\rm max} = 0.7\ {\rm cm^2\ g^{-1}}$, to the minimum opacity, $\kappa_{\rm min} = 0.07\ {\rm cm^2\ g^{-1}}$, as the temperature starts to approach $T_{\rm floor}$. This functional form and ΔT are chosen to replicate the opacity evolution in detailed numerical simulations (e.g., A. P. Nagy 2018). We note that this function is merely meant to include temperature dependence and ignores the more complex dependence on density, i.e., the opacity does not vary between layers.

We fit this model to the observed light curve as we did in Section 4.1. Compared to the one-zone model, our estimated parameters better match intuition and expectations. In particular, we infer a total ejecta mass of $0.8^{+0.5}_{-0.2}\,M_\odot$ with a ^{56}Ni mass of $0.21 \pm 0.04\ M_\odot$. We also find evidence for significant mixing, with $f_{\rm mix} = 62\% \pm 20\%$, that is, ^{56}Ni is distributed out into $\sim$60% of the mass layers. We find the cumulative mass out to the layers with ^{56}Ni is $0.6^{+0.5}_{-0.2}\,M_\odot$. The lower ^{56}Ni estimate compared to our one-zone model is driven by the high mixing, which reduces the need for a larger central ^{56}Ni as the mixed material has to overcome less adiabatic losses and diffuse through less ejecta. Comparing the Bayesian evidences, we find that the mixing model is a better fit to the data, with $\ln {\rm BF} = 1.4$ in favor of the mixing model.

Table A1
Priors Used for Each Line Fit in Section 3.4

He I/C I/Mg II Priors	
Parameter	Prior
μ_v [km s^{-1}]	$\mathcal{N}(15,000,\ 1000)$
$\log(\sigma_v$ [km s^{-1}])	$\mathcal{N}(3.5,\ 0.5)$
A	$\mathcal{U}(0,\ 5)$
$\log\left(\frac{A(2\,\mu{\rm m})}{A(1\,\mu{\rm m})}\right)$	$\mathcal{U}(-2,\ 0)$

A.2. Priors for Modeling Near-infrared Absorption Features

We give the priors used in our fitting of the 1 μm and 2 μm features in Section 3.4 in Appendix Table A1.

A.3. Tables of Observations

Here we provide a log of the photometric programs used in this work (Table A2), a lot of our spectroscopic observations (Table A3), and a table of our photometric observations of SN 2025kg (Table A4).

Table A2
Photometric Programs Employed in This Work

Telescope	Instruments	Filters	Program ID(s)	PI(s)
BlackGEM	…	*q*	Local Transient Survey	…
CFHT	MegaCam	*gri*	K1-03-00209	A. Aryan
Gemini-North	GMOS-N	*griz*	GN-2024B-Q-107	J. Rastinejad
Gemini-South	GMOS-S, FLAMINGOS2	*grizJHK*	GS-2024B-Q-105, GS-2025A-Q-107	J. Rastinejad
LBT	MODS	*g'r'i'*	IT-2024B-023	E. Maiorano
LT	IO:O	*griz*	PL24B06, PL25A25	R. Eyles-Ferris
Super Light Telescope	…	*gri*	…	T. Chen
NOT	ALFOSC	*griz*	70-301	P. Jonker
MMT	MMIRS	*K*	UAO-G206-24B	J. Rastinejad
Pan-STARRS	…	*griz*	…	S. Smartt
Lulin One-meter Telescope	…	*gri*	R09	A. Aryan
SOAR	Goodman	*riz*	SOAR2024B-016	F. Bauer
T80S	T80S-Cam	*griz*	T80S-09	C. Bom, C. Kilpatrick

Table A3
Photometric Observations of SN 2025kg

Date	δt (days)	Telescope/Instruments	Band	Exp. Time (s)	Magnitude (AB mag)	References
2025 Jan 14.93401	6.41285	LT/IO:O	*g*	6 × 200	21.11 ± 0.13	This work.
2025 Jan 15.21383	6.69268	Gemini-South/GMOS-S	*g*	60	20.94 ± 0.05	This work.
2025 Jan 15.89495	7.37379	LT/IO:O	*g*	6 × 150	20.93 ± 0.08	This work.
2025 Jan 16.47753	7.956	LOT, Lulin/Driver for Teledyne Princeton Instruments cameras	*g*	3 × 300	20.83 ± 0.11	This work.
2025 Jan 16.52491	8.00375	Gao-Mei-G (GMG)-2.4 m	*g*	…	20.78 ± 0.09	(1)
…	…	…	…	…	…	…
2025 Mar 16.00208	66.48091	Gemini-South/GMOS-S	*g*	7 × 120	22.75 ± 0.06	This work.
2025 Jan 19.08561	10.56445	BlackGEM	*q*	60	20.51 ± 0.12	This work.
…	…	…	…	…	…	…
2025 Jan 27.07300	18.55185	BlackGEM	*q*	60	20.31 ± 0.11	This work.
2025 Jan 15.17612	6.65497	Gemini-South/GMOS-S	*r*	100	20.68 ± 0.12	This work.
2025 Jan 15.60866	7.0875	GMG-2.4 m	*r*	…	20.75 ± 0.16	(1)
…	…	…	…	…	…	…
2025 Mar 16.01389	66.49272	Gemini-South/GMOS-S	*r*	7 × 120	22.19 ± 0.07	This work.
2025 Jan 19.67752	11.15636	DFOT	*R*	12 × 300	19.89 ± 0.04	This work.
2025 Jan 15.44627	6.92512	ATLAS	*o*	7 × 30	> 19.70	This work.
…	…	…	…	…	…	…
2025 Feb 04.46553	26.94438	ATLAS	*o*	8 × 30	20.23 ± 0.19	This work.
2025 Jan 15.22278	6.70162	Gemini-South/GMOS-S	*i*	60	20.95 ± 0.07	This work.
…	…	…	…	…	…	…
2025 Mar 16.02813	66.50699	Gemini-South/GMOS-S	*i*	7 × 100	22.04 ± 0.09	This work.
2025 Jan 14.96824	6.44708	LT/IO:O	*z*	6 × 200	21.06 ± 0.18	This work.
…	…	…	…	…	…	…
2025 Mar 01.24099	51.71984	Pan-STARRS	*z*	1800	21.74 ± 0.33	This work.
2025 Mar 16.23999	66.71884	Pan-STARRS	*z*	1800	> 21.41	This work.
2025 Jan 20.03253	11.51137	Gemini-South/F2	*J*	26 × 30	20.76 ± 0.03	This work.
2025 Jan 29.10275	20.58159	Gemini-South/F2	*J*	25 × 30	20.61 ± 0.06	This work.
2025 Jan 20.05285	11.53169	Gemini-South/F2	*H*	38 × 10	21.25 ± 0.11	This work.
…	…	…	…	…	…	…
2025 Mar 08.00869	58.48752	Gemini-South/F2	*H*	41 × 10	22.25 ± 0.19	This work.
2025 Jan 20.14749	11.62633	MMT/MMIRS	*K*	93 × 20	21.45 ± 0.15	This work.
2025 Jan 29.11899	20.59782	Gemini-South/F2	*K*	38 × 10	21.02 ± 0.07	This work.

Note. Observations are not corrected for Galactic nor local extinction. Times are presented in the observer frame.
References. (1) F. F. Song et al. (2025).

(This table is available in its entirety in machine-readable form in the online article.)

Table A4
Log of SN 2025kg Spectroscopic Observations

Date and Midtime (UTC)	δt (days)	Tel.	Instrument	Exp. Time (s)	Wavelength Range (Å)
2025-01-19 01:41:47	10.5	Gemini-South	GMOS	4 × 400	4300–8400
2025-01-19 07:42:41	10.8	Gemini-North	GMOS	4 × 1200	4800–9000
2025-01-19 21:17:24	11.4	GTC	OSIRIS	3 × 1200, 3 × 900	3600–9500
2025-01-22 01:12:58	13.5	Gemini-South	GMOS	4 × 250	4300–9000
2025-01-22 04:10:00	13.7	LBT	MODS	2 × 900	3200-10000
2025-01-22 05:57:25	13.7	Gemini-North	GNIRS	11 × 300	7000–21400
2025-01-24 02:25:46	15.6	VLT	MUSE	4 × 608	4700–9300
2025-01-25 01:35:30	16.5	Gemini-South	GMOS	4 × 400	4300–8400
2025-01-25 16:43:34	17.2	JWST	NIRSpec	6302.4	6000–53000
2025-01-26 05:45:45	17.7	Keck I	LRIS	3 × 900	3000–10200
2025-01-29 06:25:50	20.7	Gemini-South	GMOS	4 × 800	4900–9400
2025-01-29 05:25:51	20.7	Keck I	LRIS	2 × 900	3000–10200
2025-02-05 21:02:32	28.4	GTC	OSIRIS	3 × 900	3200–9400
2025-02-20 01:14:56	42.5	Gemini-South	GMOS	4 × 800	5500–9400
2025-02-26 05:57:25	47.4	Keck I	LRIS	3 × 1200	3000–8900

ORCID iDs

Jillian C. Rastinejad https://orcid.org/0000-0002-9267-6213
Andrew J. Levan https://orcid.org/0000-0001-7821-9369
Peter G. Jonker https://orcid.org/0000-0001-5679-0695
Charles D. Kilpatrick https://orcid.org/0000-0002-5740-7747
Christopher L. Fryer https://orcid.org/0000-0003-2624-0056
Nikhil Sarin https://orcid.org/0000-0003-2700-1030
Benjamin P. Gompertz https://orcid.org/0000-0002-5826-0548
Chang Liu https://orcid.org/0000-0002-7866-4531
Rob A. J. Eyles-Ferris https://orcid.org/0000-0002-8775-2365
Wen-fai Fong https://orcid.org/0000-0002-7374-935X
Eric Burns https://orcid.org/0000-0002-2942-3379
James H. Gillanders https://orcid.org/0000-0002-8094-6108
Ilya Mandel https://orcid.org/0000-0002-6134-8946
Daniele Bjørn Malesani https://orcid.org/0000-0002-7517-326X
Paul T. O'Brien https://orcid.org/0000-0002-5128-1899
Nial R. Tanvir https://orcid.org/0000-0003-3274-6336
Kendall Ackley https://orcid.org/0000-0002-8648-0767
Amar Aryan https://orcid.org/0000-0002-9928-0369
Franz E. Bauer https://orcid.org/0000-0002-8686-8737
Steven Bloemen https://orcid.org/0000-0002-6636-921X
Thomas de Boer https://orcid.org/0000-0001-5486-2747
Clécio R. Bom https://orcid.org/0000-0003-4383-2969
Jennifer A. Chacón https://orcid.org/0009-0000-6374-3221
Ken Chambers https://orcid.org/0000-0001-6965-7789
Ting-Wan Chen https://orcid.org/0000-0002-1066-6098
Ashley A. Chrimes https://orcid.org/0000-0001-9842-6808
Joyce N. D. van Dalen https://orcid.org/0009-0007-6927-7496
Valerio D'Elia https://orcid.org/0000-0002-7320-5862
Massimiliano De Pasquale https://orcid.org/0000-0002-4036-7419
Michael D. Fulton https://orcid.org/0000-0003-1916-0664
Paul J. Groot https://orcid.org/0000-0002-4488-726X
Rahul Gupta https://orcid.org/0000-0003-4905-7801
Dieter H. Hartmann https://orcid.org/0000-0002-8028-0991
Agnes P. C. van Hoof https://orcid.org/0009-0005-5404-2745
Mark E. Huber https://orcid.org/0000-0003-1059-9603
Luca Izzo https://orcid.org/0000-0001-9695-8472
Wynn Jacobson-Galan https://orcid.org/0000-0003-1103-3409
Páll Jakobsson https://orcid.org/0000-0002-9404-5650
Albert Kong https://orcid.org/0000-0002-5105-344X
Tanmoy Laskar https://orcid.org/0000-0003-1792-2338
Thomas B. Lowe https://orcid.org/0000-0002-9438-3617
Eugene A. Magnier https://orcid.org/0000-0002-7965-2815
Elisabetta Maiorano https://orcid.org/0000-0003-2593-4355
Antonio Martin-Carrillo https://orcid.org/0000-0001-5108-0627
Daniel Mata Sánchez https://orcid.org/0000-0003-0245-9424
Matt Nicholl https://orcid.org/0000-0002-2555-3192
Christopher J. Nixon https://orcid.org/0000-0002-2137-4146
Samantha R. Oates https://orcid.org/0000-0001-9309-7873
Gregory Paek https://orcid.org/0000-0002-6639-6533
Jesse Palmerio https://orcid.org/0000-0002-9408-1563
Diego Paris https://orcid.org/0000-0002-7409-8114
Daniëlle L. A. Pieterse https://orcid.org/0000-0003-3114-2733
Giovanna Pugliese https://orcid.org/0000-0003-3457-9375
Jonathan A. Quirola Vasquez https://orcid.org/0000-0001-8602-4641
Jan van Roestel https://orcid.org/0000-0002-2626-2872
Andrea Rossi https://orcid.org/0000-0002-8860-6538
Alicia Rouco Escorial https://orcid.org/0000-0003-3937-0618
Ruben Salvaterra https://orcid.org/0000-0002-9393-8078
Benjamin Schneider https://orcid.org/0000-0003-4876-7756
Stephen J. Smartt https://orcid.org/0000-0002-8229-1731
Ken Smith https://orcid.org/0000-0001-9535-3199
Ian A. Smith https://orcid.org/0000-0001-8605-5608
Shubham Srivastav https://orcid.org/0000-0003-4524-6883
Manuel A. P. Torres https://orcid.org/0000-0002-5297-2683
Chiara Ventura https://orcid.org/0009-0009-9751-9215
Richard Wainscoat https://orcid.org/0000-0002-1341-0952
Yi-Jung Yang https://orcid.org/0000-0001-9108-573X
Sheng Yang https://orcid.org/0000-0002-2898-6532

References

Aktar, R., Das, S., Nandi, A., & Sreehari, H. 2017, MNRAS, 471, 4806
Alp, D., & Larsson, J. 2020, ApJ, 896, 39
Arnett, W. D. 1982, ApJ, 253, 785
Ashton, G., Hübner, M., Lasky, P. D., et al. 2019, ApJS, 241, 27
Bauer, F. E., Treister, E., Schawinski, K., et al. 2017, MNRAS, 467, 4841

Bersten, M. C., Benvenuto, O., & Nomoto, K. 2014, in IAU Symp. 296, Supernova Environmental Impacts, ed. A. Ray & R. A. McCray (San Francisco, CA: ASP), 58
Bochenek, A., Xu, D., Zhu, Z. P., et al. 2024, GCN, 37039, 1
Bright, J. S., Carotenuto, F., Fender, R., et al. 2025, ApJ, 981, 48
Buchner, J., Georgakakis, A., Nandra, K., et al. 2014, A&A, 564, A125
Bufano, F., Pian, E., Sollerman, J., et al. 2012, ApJ, 753, 67
Busmann, M., O'Connor, B., Sommer, J., et al. 2025, arXiv:2503.14588
Campana, S., Mangano, V., Blustin, A. J., et al. 2006, Natur, 442, 1008
Cano, Z., Bersier, D., Guidorzi, C., et al. 2011, ApJ, 740, 41
Cano, Z., Izzo, L., de Ugarte Postigo, A., et al. 2017, A&A, 605, A107
Chornock, R., Berger, E., Levesque, E. M., et al. 2010, arXiv:1004.2262
Clocchiatti, A., Suntzeff, N. B., Covarrubias, R., & Candia, P. 2011, AJ, 141, 163
Cooke, B. A. 1976, Natur, 261, 564
Corsi, A., Gal-Yam, A., Kulkarni, S. R., et al. 2016, ApJ, 830, 42
Dainotti, M. G., De Simone, B., Islam, K. M., et al. 2022, ApJ, 938, 41
Dessart, L., Gutiérrez, C. P., Ercolino, A., Jin, H., & Langer, N. 2024, A&A, 685, A169
Dessart, L., Yoon, S.-C., Aguilera-Dena, D. R., & Langer, N. 2020, A&A, 642, A106
Dey, A., Schlegel, D. J., Lang, D., et al. 2019, AJ, 157, 168
Drout, M. R., Soderberg, A. M., Gal-Yam, A., et al. 2011, ApJ, 741, 97
Evans, P. A., Beardmore, A. P., Page, K. L., et al. 2007, A&A, 469, 379
Evans, P. A., Beardmore, A. P., Page, K. L., et al. 2009, MNRAS, 397, 1177
Eyles-Ferris, R. A. J., Jonker, P. G., Levan, A. J., et al. 2025, ApJL, 988, L14
Finneran, G., & Martin-Carrillo, A. 2024, arXiv:2411.12574
Fitzpatrick, E. L. 1999, PASP, 111, 63
Flewelling, H. A., Magnier, E. A., Chambers, K. C., et al. 2020, ApJS, 251, 7
Foley, R. J., Papenkova, M. S., Swift, B. J., et al. 2003, PASP, 115, 1220
Fontana, A., Dunlop, J. S., Paris, D., et al. 2014, A&A, 570, A11
Frederiks, D., Lysenko, A., Ridnaia, A., et al. 2024, GCN, 37071, 1
Freudling, W., Romaniello, M., Bramich, D. M., et al. 2013, A&A, 559, A96
Frey, L. H., Fryer, C. L., & Young, P. A. 2013, ApJL, 773, L7
Fryer, C. L. 1999, ApJ, 522, 413
Fryer, C. L., Burns, E., Ho, A. Y. Q., et al. 2025, ApJ, 986, 185
Fryer, C. L., Fontes, C. J., Warsa, J. S., et al. 2020, ApJ, 898, 123
Fryer, C. L., Keiter, P. A., Sharma, V., et al. 2023, arXiv:2312.16677
Fryer, C. L., & Woosley, S. E. 1998, ApJL, 502, L9
Galama, T. J., Vreeswijk, P. M., van Paradijs, J., et al. 1998, Natur, 395, 670
Gargiulo, A., Fumana, M., Bisogni, S., et al. 2022, MNRAS, 514, 2902
Glennie, A., Jonker, P. G., Fender, R. P., Nagayama, T., & Pretorius, M. L. 2015, MNRAS, 450, 3765
Greiner, J., Mazzali, P. A., Kann, D. A., et al. 2015, Natur, 523, 189
Grichener, A. 2025, Ap&SS, 370, 11
Groot, P. J., Bloemen, S., Vreeswijk, P. M., et al. 2024, PASP, 136, 115003
Harutyunyan, A. H., Pfahler, P., Pastorello, A., et al. 2008, A&A, 488, 383
Heise, J., Zand, J. I., Kippen, R. M., & Woods, P. M. 2001, in Gamma-ray Bursts in the Afterglow Era, ed. E. Costa, F. Frontera, & J. Hjorth (Berlin: Springer), 16
Hirai, R. 2023, MNRAS, 523, 6011
Hirai, R., Podsiadlowski, P., & Yamada, S. 2018, ApJ, 864, 119
Hirai, R., Sato, T., Podsiadlowski, P., Vigna-Gómez, A., & Mandel, I. 2020, MNRAS, 499, 1154
Hiramatsu, D., Arcavi, I., Burke, J., et al. 2020, TNSCR, 2020, 1
Ho, A. Y. Q., Kulkarni, S. R., Perley, D. A., et al. 2020, ApJ, 902, 86
Hu, Y. D., Castro-Tirado, A. J., Kumar, A., et al. 2021, A&A, 646, A50
Izzo, L., Auchettl, K., Hjorth, J., et al. 2020, A&A, 639, L11
Izzo, L., de Ugarte Postigo, A., Maeda, K., et al. 2019, Natur, 565, 324
Izzo, L., Martin-Carrillo, A., Malesani, D. B., et al. 2025, GCN, 39851, 1
Jonker, P. G., Glennie, A., Heida, M., et al. 2013, ApJ, 779, 14
Khatami, D. K., & Kasen, D. N. 2019, ApJ, 878, 56
Labrie, K., Anderson, K., Cárdenes, R., Simpson, C., & Turner, J. E. H. 2019, in ASP Conf. Ser. 523, Astronomical Data Analysis Software and Systems XXVII, ed. P. J. Teuben et al. (San Francisco, CA: ASP), 321
Levan, A. J., Gompertz, B. P., Salafia, O. S., et al. 2024a, Natur, 626, 737
Levan, A. J., Jonker, P. G., Saccardi, A., et al. 2024b, arXiv: 2404.16350
Levan, A. J., Malesani, D. B., Jonker, P. G., et al. 2025a, GCN, 39278, 1
Levan, A. J., Quirola-Vasquez, J. A., Rastinejad, J. C., et al. 2024c, GCN, 38593, 1
Levan, A. J., Rastinejad, J. C., Malesani, D. B., et al. 2025b, GCN, 38987, 1
Levan, A. J., Tanvir, N. R., Starling, R. L. C., et al. 2014, ApJ, 781, 13
Li, R. Z., Chen, X. L., Chatterjee, K., et al. 2025a, GCN, 38861, 1
Li, W. X., Zhu, Z. P., Zou, X. Z., et al. 2025b, arXiv:2504.17034
Liljegren, S., Jerkstrand, A., Barklem, P. S., et al. 2023, A&A, 674, A184
Lin, D., Irwin, J. A., Berger, E., & Nguyen, R. 2022, ApJ, 927, 211
Liu, C., Miller, A. A., Polin, A., et al. 2023, ApJ, 946, 83
Liu, Y., Sun, H., Xu, D., et al. 2025, NatAs, 9, 564
Lucy, L. B. 1991, ApJ, 383, 308
Magnier, E. A., & Cuillandre, J. C. 2004, PASP, 116, 449
Maguire, K., Taubenberger, S., Sullivan, M., & Mazzali, P. A. 2016, MNRAS, 457, 3254
Margutti, R., Metzger, B. D., Chornock, R., et al. 2019, ApJ, 872, 18
Matheson, T., Garnavich, P. M., Stanek, K. Z., et al. 2003, ApJ, 599, 394
Matzner, C. D., & McKee, C. F. 1999, ApJL, 526, L109
Meikle, W. P. S., Allen, D. A., Spyromilio, J., & Varani, G. F. 1989, MNRAS, 238, 193
Metzger, B. D. 2019, LRR, 23, 1
Mirabal, N., Halpern, J. P., An, D., Thorstensen, J. R., & Terndrup, D. M. 2006, ApJL, 643, L99
Modjaz, M., Blondin, S., Kirshner, R. P., et al. 2014, AJ, 147, 99
Modjaz, M., Liu, Y. Q., Bianco, F. B., & Graur, O. 2016, ApJ, 832, 108
Modjaz, M., Li, W., Butler, N., et al. 2009, ApJ, 702, 226
Modjaz, M., Stanek, K. Z., Garnavich, P. M., et al. 2006, ApJL, 645, L21
Nagy, A. P. 2018, ApJ, 862, 143
Niblett, A. E., Fryer, D. A., & Fryer, C. L. 2025, arXiv:2501.15702
Nicholl, M., Srivastav, S., Fulton, M. D., et al. 2023, ApJL, 954, L28
Novara, G., Esposito, P., Tiengo, A., et al. 2020, ApJ, 898, 37
O'Connor, B., Pasham, D., Andreoni, I., et al. 2025, ApJL, 979, L30
Olivares, E. F., Greiner, J., Schady, P., et al. 2012, A&A, 539, A76
Owocki, S. P., & Rybicki, G. B. 1984, ApJ, 284, 337
Patat, F., Cappellaro, E., Danziger, J., et al. 2001, ApJ, 555, 900
Perley, D. A., Cenko, S. B., Corsi, A., et al. 2014, ApJ, 781, 37
Perley, D. A., Mazzali, P. A., Yan, L., et al. 2019, MNRAS, 484, 1031
Pian, E., Amati, L., Antonelli, L. A., et al. 2000, ApJ, 536, 778
Pian, E., Mazzali, P. A., Masetti, N., et al. 2006, Natur, 442, 1011
Planck Collaboration, Aghanim, N., Akrami, Y., et al. 2020, A&A, 641, A6
Prentice, S. J., Maguire, K., Smartt, S. J., et al. 2018, ApJL, 865, L3
Prochaska, J., Hennawi, J., Westfall, K., et al. 2020, JOSS, 5, 2308
Puls, J., Vink, J. S., & Najarro, F. 2008, A&ARv, 16, 209
Quataert, E., Fernández, R., Kasen, D., Klion, H., & Paxton, B. 2016, MNRAS, 458, 1214
Quirola-Vásquez, J., Bauer, F. E., Jonker, P. G., et al. 2022, A&A, 663, A168
Quirola-Vásquez, J., Bauer, F. E., Jonker, P. G., et al. 2023, A&A, 675, A44
Rastinejad, J. C., Fong, W., Levan, A. J., et al. 2024, ApJ, 968, 14
Rastinejad, J. C., Gompertz, B. P., Levan, A. J., et al. 2022, Natur, 612, 223
Ravasio, M. E., Burns, E., Wilson-Hodge, C., Jonker, P. G. & Fermi-GBM Team 2025, GCN, 39146, 1
Reichert, M., Obergaulinger, M., Aloy, M. Á., et al. 2023, MNRAS, 518, 1557
Rest, A., Stubbs, C., Becker, A. C., et al. 2005, ApJ, 634, 1103
Rodríguez, Ó., Maoz, D., & Nakar, E. 2023, ApJ, 955, 71
Ror, A. K., Gupta, A., Kiran Pandey, S. B., & Mishra, K. 2025, GCN, 39002, 1
Sakamoto, T., Lamb, D. Q., Kawai, N., et al. 2005, ApJ, 629, 311
Santos, A., Kilpatrick, C. D., Bom, C. R., et al. 2024, MNRAS, 529, 59
Sarin, N., Hübner, M., Omand, C. M. B., et al. 2024, MNRAS, 531, 1203
Schlafly, E. F., & Finkbeiner, D. P. 2011, ApJ, 737, 103
Science Software Branch at STScI 2012, PyRAF: Python Alternative for IRAF, Astrophysics Source Code Library, ascl:1207.011
Shahbandeh, M., Ashall, C., Hoeflich, P., et al. 2024, arXiv:2401.14474
Shahbandeh, M., Hsiao, E. Y., Ashall, C., et al. 2022, ApJ, 925, 175
Siegel, D. M., Barnes, J., & Metzger, B. D. 2019, Natur, 569, 241
Siegel, D. M., & Metzger, B. D. 2017, PhRvL, 119, 231102
Skrutskie, M. F., Cutri, R. M., Stiening, R., et al. 2006, AJ, 131, 1163
Soderberg, A. M., Berger, E., Kasliwal, M., et al. 2006, ApJ, 650, 261
Soderberg, A. M., Berger, E., Page, K. L., et al. 2008, Natur, 453, 469
Sollerman, J., Cumming, R. J., & Lundqvist, P. 1998, ApJ, 493, 933
Song, F. F., Li, R. Z., Wang, B. T., et al. 2025, GCN, 38972, 1
Srinivasaragavan, G. P., Hamidani, H., Schroeder, G., et al. 2025, arXiv:2504.17516
Srinivasaragavan, G. P., Yang, S., Anand, S., et al. 2024, ApJ, 976, 71
Srivastav, S., Chen, T. W., Gillanders, J. H., et al. 2025, ApJL, 978, L21
Sun, H., Li, W. X., Liu, L. D., et al. 2024, arXiv:2410.02315
Sun, H., Zhang, B., & Li, Z. 2015, ApJ, 812, 33
Surman, R., McLaughlin, G. C., & Hix, W. R. 2006, ApJ, 643, 1057
Taddia, F., Sollerman, J., Fremling, C., et al. 2019, A&A, 621, A71
Tinyanont, S., Foley, R. J., Taggart, K., et al. 2024, PASP, 136, 014201
Tonry, J. L., Denneau, L., Heinze, A. N., et al. 2018, PASP, 130, 064505
Troja, E., Fryer, C. L., O'Connor, B., et al. 2022, Natur, 612, 228
Tucker, M. A., Shappee, B. J., Vallely, P. J., et al. 2020, MNRAS, 493, 1044
van Dalen, J. N. D., Levan, A. J., Jonker, P. G., et al. 2025, ApJL, 982, L47

van Dokkum, P. G. 2001, PASP, 113, 1420
Weaver, R., McCray, R., Castor, J., Shapiro, P., & Moore, R. 1977, ApJ, 218, 377
Woosley, S. E., Heger, A., & Weaver, T. A. 2002, RvMP, 74, 1015
Xiang, D., Wang, X., Lin, W., et al. 2021, ApJ, 910, 42
Xu, D., Zhu, Z. P., Liu, X., et al. 2025, GCN, 38984, 1
Yan, L., Lunnan, R., Perley, D. A., et al. 2017, ApJ, 848, 6
Yang, J., Ai, S., Zhang, B.-B., et al. 2022, Natur, 612, 232
Yang, Y.-H., Becerra, R. L., Watson, A. M., et al. 2025, GCN, 39305, 1
Yaron, O., & Gal-Yam, A. 2012, PASP, 124, 668
Yin, Y.-H. I., Zhang, B.-B., Yang, J., et al. 2024, ApJL, 975, L27
Yuan, W., Zhang, C., Chen, Y., & Ling, Z. 2022, in Handbook of X-ray and Gamma-ray Astrophysics, ed. C. Bambi & A. Sangangelo (Berlin: Springer), 86
Yuan, W., Zhang, C., Feng, H., et al. 2015, arXiv:1506.07735
Zenati, Y., Siegel, D. M., Metzger, B. D., & Perets, H. B. 2020, MNRAS, 499, 4097
Zhang, W. J., Mao, X., Zhang, W. D., et al. 2024, GCN, 35931, 1
Zhu, J.-P., Liu, L.-D., Yu, Y.-W., et al. 2024, ApJL, 970, L42
Zou, X., Liu, C., Kumar, B., et al. 2025, GCN, 38914, 1